ARTICLE

Engineering the interfaces in water-splitting photoelectrodes – an overview of the technique development

Received 00th January 20xx,
Accepted 00th January 20xx

DOI: 10.1039/x0xx00000x

Yawen Dai,[a] Jie Yu [a], Chun Cheng,[a] Peng Tan[b] and Meng Ni *[a]

Photoelectrochemical (PEC) water splitting offers an attractive option for solar fuel production to solve the global energy crisis and environmental issues, but the present low efficiency hinders its practical application. Interface engineering has been demonstrated to be critical for developing high-performance photoelectrodes for efficient water splitting. However, effective interface engineering requires insightful understanding of the interfacial thermodynamics, carrier dynamics, and surface reaction mechanisms, all of which essentially depend on the advances of study techniques. Herein, electrochemical and optical spectroscopic techniques applied for interface studies in PEC systems are overviewed. The fundamentals and data analysis methods of each technique are introduced, in company with representative achievements in understanding the PEC interfaces. Both conventional and newly developed techniques are included, with some discussions on their advantages and limitations. Finally, a perspective on the challenges and the future progress of techniques for PEC interface studies is also given. This review could inspire the further technique development and mechanistic understanding of PEC water splitting.

1. Introduction

Developing sustainable and green energy technologies is urgent for modern society given the increasing global energy demand and environment pollution, as well as the decreasing reserves of fossil fuels.[1,2] H_2 is an attractive new energy source due to its clean combustion product and high gravimetric heating value. Solar water splitting using semiconductors (SCs) as photoabsorber provides a convenient way to store the inexhaustible but intermittent solar energy in H_2. Hence, it has been regarded as one of the most promising technologies to alleviate the energy and pollution problems.[3-5] There are three types of device configuration for solar water splitting, namely photocatalysis (PC) (Figure 1a and 1d), photoelectrochemical (PEC) cell (Figure 1b and 1e), and photovoltaic (PV)-electrocatalyst (EC) tandem cell (Figure 1c and 1f).[5,6] The features of the three solar water splitting systems are listed in Table 1. PEC cells have attracted much interest due to the lower cost as compared to that of PV-EC, as well as the higher energy conversion efficiency and easier gas collection as compared to those of PC.[5] However, the record solar to hydrogen efficiency of PEC cells (without PV component) is 3.7%, which is far lower than the industrialization demand of 10%, hindering the practical application.[7] PEC water splitting consists of two half reactions, which are oxygen evolution reaction (OER) on photoanodes and hydrogen evolution reaction (HER) on photocathodes. Compared to HER, OER is more difficult due to the 4-hole/4-electron-participated process that significantly limits the overall efficiency of PEC.[8] Hence, we overview representative works on photoanodes in this review.

It has been demonstrated that PEC performance largely depends on interface engineering in both thermodynamic and kinetic aspects. Thermodynamically, photovoltage generation is dominated by the Schottky barrier height at the semiconductor (SC)-electrolyte interface, or the interfaces between solid state materials in buried-junction-type photoelectrodes.[9,10] The photovoltage can be enlarged by coating overlayers to passivate the surface states of SCs, or by modulating the work function of metals on SCs.[11,12] On the kinetic side, the heteroatoms and defects of SC can play complex roles at the electrode-electrolyte

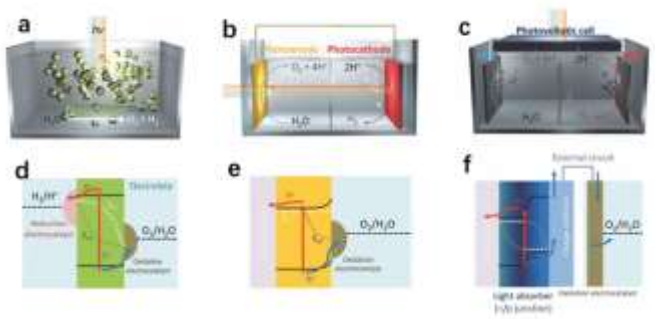

Figure 1. System configurations and charge flows under illumination of (a) (d) PC, (b) (e) PEC, and (c) (f) PV-EC systems. Reproduced with permission from ref 5. Copyright 2019 The Royal Society of Chemistry.

[a] Department of Building and Real Estate, The Hong Kong Polytechnic University, Hung Hom, Kowloon, Hong Kong 999077, China.
[b] Department of Thermal Science and Energy Engineering, University of Science and Technology of China, Hefei 230026, Anhui, China.
* Corresponding author.

Table 1. Key features of PC, PEC, and PV-EC systems

System	Configuration	H_2 and O_2 generation	System complexity	Efficiency
PC	Photocatalysts dispersed in solution	Both from photocatalyst particles	Low	Low
PEC	Photocathode (p-type) in tandem with photoanode (n-type) immersed in solution	Separately from photocathode and photoanode	Moderate	Moderate
PV-EC	PV component (out of solution) in tandem with electrocatalysts	Separately from ECs for HER and OER	High	High

interface. They can act as either charge transfer intermediates to promote the photocurrent, or charge recombination centres to decrease the photocurrent.[13,14] Besides, to facilitate charge separation, internal electric fields can be constructed by fabricating heterojunctions with suitable band alignment or polarization effect.[15,16] Moreover, ECs are always deposited on SCs to accelerate surface redox reactions, but an active EC cannot guarantee improved PEC activity since the charge accumulation in ECs may reduce the utilization of photocarriers.[17,18] For the above modifications, new interfaces appear in the photoelectrodes and complicates the relevant interfacial charge behaviour. The effect of these modification on the final PEC performance is substantially dominated by the interface properties.[19] Therefore, gaining insightful understanding on PEC interfaces is of high significance, which can provide guidance for interface engineering towards more highly efficient photoelectrodes.

Several reviews have summarized the recent advances in the interface mechanism study in PEC systems, highlighting the key issues involving interfaces between the photoabsorber, modification layer, and electrolyte.[19-22] There are several obstacles in studying the interface problems in PEC systems. First, it is difficult to glean objective interface information from the complex reaction conditions which simultaneously combines the light illumination, applied bias, and the solid-liquid junction environment. Second, it is hard to distinguish the charge behaviour at different interfaces in the multilayer photoelectrodes, especially for nanostructured photoelectrodes with rather thin or inhomogeneous modification layers. Third, it is also a challenge to monitor the interfacial carrier dynamics at an ultrafast time scale. Hence, a deep understanding on the interfaces in PEC systems is essentially limited by the technique development.

In this review, instead of providing interface engineering strategies like previous reviews, we intend to focus on the development of techniques for studying PEC interface problems. According to the output signals, the techniques are generally categorized into two broad groups: (1) electrochemical techniques and (2) optical spectroscopic techniques. In each part, the fundamental of techniques will be introduced, followed by examples of their application in PEC interface studies and data analysis. We will overview the conventionally used and easily accessible techniques, as well as the newly developed techniques which can achieve more accurate spatial and time resolution. The strengths and weaknesses of each technique are also discussed, which may help the readers to select appropriate techniques and evaluate the data reliability in certain conditions. Last, we briefly summarize the challenges and provide suggestions for the future technique development in PEC interface study.

2. Electrochemical techniques

2.1 Frequency-modulated electrochemical techniques

2.1.1 Photoelectrochemical impedance spectroscopy (PEIS). Electrochemical impedance spectroscopy (EIS) is a common tool for analyzing the electric and interface properties of materials in electrochemistry.[23] For the EIS measurement, a small amplitude of AC potential perturbation ($\tilde{V}$) is applied around a constant applied potential, and the resulting oscillating current ($\tilde{\imath}$) response is recorded, from which the impedance (Z) is calculated by $Z= \tilde{V}/\tilde{\imath}$. The impedance is measured as a function of frequency (f).[24] PEIS is the same as EIS excepted for "P" is inserted in the name of technique to emphasize the illumination condition.[25] PEIS spectra can be displayed as phase vs. f (named as Bode plots, Figure 2a), or Z'' vs. Z' (named as Nyquist plots, Figure 2b), where Z'' and Z' represent the imaginary and real components of the impedance, respectively. Two methods to analyse the interfaces in PEC process through PEIS will be introduced in this part.

The first method is to directly analyse the measured Bode or Nyquist plots without fitting models. Charge behaviour at different interfaces can be identified from the frequency-sensitive Bode peaks, while the charge transport and transfer resistances can be indicated by the radius of semicircles in Nyquist plots.[26-29] In a Bode plot, the frequency value of each peak corresponds to the time scale of the relevant process, and the phase value reflects charge accumulation at a certain interface and helps to determine the limiting process of the PEC activity.[18,26,30] Gong *et al* studied the Bode plots of α-Fe_2O_3 photoanodes coated by cobalt oxides, in which charge transport and transfer across different regions are identified according to the peak frequencies (Figure 2a). By scrutinizing the peaks corresponding to the electrode/electrolyte interface, they concluded that the interfacial charge transfer was slowed by coating CoO as indicated by the smaller peak frequency of α-Fe_2O_3/CoO than that of the bare α-Fe_2O_3.[18] Moreover, from the phase value of the peaks, it can be concluded that the PEC

activity is limited by bulk charge transport in bare α-Fe_2O_3 and α-Fe_2O_3/Co_3O_4, while the electrode/electrolyte interfacial charge transfer in is the limiting process in α-Fe_2O_3/CoO.[18] Similar analysis was also applied in α-Fe_2O_3/NiOOH photoanodes.[26,30] In a typical Nyquist plot of a photoanode, the two arcs at high and low frequency regions are ascribed to bulk charge transport and electrode/electrolyte interfacial charge transfer, respectively.[31,32] Zhao *et al* measured the Nyquist plots of a hematite photoanode at 1.23 V_{RHE} (potential versus reversible hydrogen electrode), finding that hematite shows large low frequency arc in D_2O than in H_2O under mild alkaline PEC conditions (Figure 2b). This study indicates the larger interfacial charge transfer resistance induced by D^+ than that by H^+, which supports that the rate-determining step of the water oxidation on the photoanode undergoes a the concerted proton-electron transfer mechanism.[27]

The second method is to fit the PEIS spectra using an equivalent circuit, through which the charge behaviour in a photoelectrode is modelled by circuit elements such as capacitors and resistors, etc. Figure 2c shows the commonly used equivalent circuit for hematite photoanodes, consisting of a capacitance of the bulk space charge layer (C_{bulk}), a surface state capacitance (C_{trap}), a series resistance (R_s), a resistance of hole trapping to the surface (R_{trap}), and a resistance of hole transfer from surface states to the solution ($R_{ct,trap}$).[24,33,34] Using PEIS fitting, Hamann's group evidenced that holes are initially trapped to the surface states of hematite under PEC conditions, accumulating to achieve a critical number of surface holes that are required for the subsequent hole transfer step to proceed.[24] It was observed that the C_{trap} values display a Gaussian distribution as a function of the applied potential, with a peak corresponding to a dip in $R_{ct,trap}$ (Figure 2d). Moreover, the peak of C_{trap} and the dip of $R_{ct,trap}$ coincide with the onset potential of the photocurrent (Figure 2d), indicating that holes are stored in the surface states, from which the hole transfer takes place.[34] The surface states were found to be influenced by dopants in semiconductors, where an optimal doping level is required for a maximum overlapping between surface and water states to benefit the hole transfer from the photoanode to electrolyte for water oxidation.[35]

In addition, the equivalent circuit is also applicable when ECs are integrated. In this case, ECs provide a more favourable pathway for hole storage and transfer, and thus C_{trap} and $R_{ct,trap}$ are replaced by C_{cat} and $R_{ct,cat}$, respectively.[36,37] Hamann's group investigated the α-Fe_2O_3/CoPi photoanode, finding that C_{CoPi} increases with the CoPi thickness, which demonstrates the role of CoPi as a hole collector during PEC process.[36] Their group also studied the α-Fe_2O_3/$Ni_{1-x}Fe_xO_y$ system by fitting the PEIS curve with an equivalent circuit model, revealing that the Fe-rich EC efficiently collects holes and circumvents recombination at the α-Fe_2O_3 surface, while the Ni-rich one leads to deleterious interface trap states that act as recombination centres which pin the EC potential.[37]

Furthermore, the rate constants of interfacial charge transfer (k_{ct}) and recombination (k_{rec}) can be calculated from the PEIS fitting results according to the model developed by

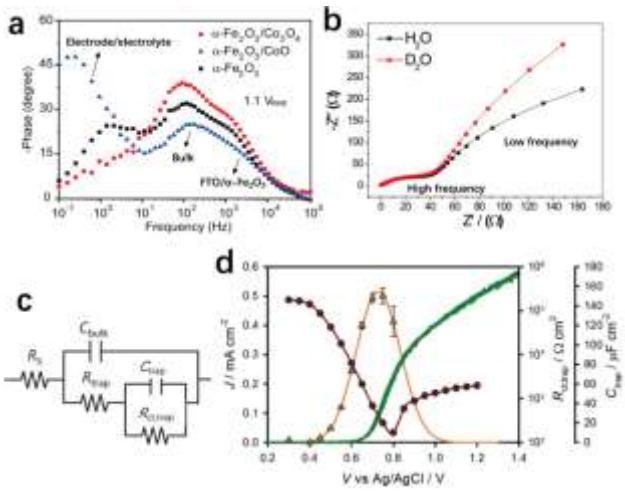

Figure 2. (a) PEIS-Bode plots of α-Fe_2O_3/Co_3O_4, α-Fe_2O_3/CoO, and α-Fe_2O_3 photoanodes. Reproduced with permission from ref. [18]. Copyright 2019 American Chemical Society. (b) Nyquist plots for PEIS conducted in H_2O and D_2O for a hematite photoanode at 1.23 V_{RHE} in an unbuffered electrolyte at pH/pD 10.0. Reproduced with permission from ref. [27]. Copyright 2016 American Chemical Society. (c) The typical equivalent circuit for PEIS fitting of hematite-based photoanodes. (d) Photocurrent-potential curve (green solid line), C_{trap} (orange triangles), and $R_{ct,trap}$ (red circles) values obtained for a 60 nm hematite electrode under 1 sun illumination and pH 6.9 electrolyte. Reproduced with permission from ref. [34]. Copyright 2012 American Chemical Society.

Peter and coworkers.[38-40] For the case where the semiconductor space charge capacitance is much smaller than the Helmholtz capacitance, k_{ct} is in reciprocal relation to the time constant of the low frequency arc:

$$k_{ct} = \frac{1}{C_{LF}R_{LF}} \quad (1)$$

$$k_{rec} = \frac{R_{LF}}{R_{HF}}k_{ct} \quad (2)$$

where C_{LF} and R_{LF} represent the capacitance and resistance of the low frequency arc, respectively, and R_{HF} stands for the resistance of the high frequency arc.

By comparing the of rate constants of α-Fe_2O_3 photoanodes with and without CoPi coating, Gamelin *et al* demonstrated the mechanism for the CoPi induced PEC activity improvement. Although CoPi slows the water oxidation kinetics to some extent, it slows the interfacial charge recombination more significantly, resulting in a net enhancement of the photocurrent.[41] Zhang *et al* demonstrated that inserting a GaO_x interlayer between α-Fe_2O_3 and the $CoFeO_x$ EC can realize simultaneous increase of k_{ct} and decrease of k_{rec}, which are more preferred for the PEC activity promotion.[39]

2.1.2 Intensity modulated photocurrent/photovoltage spectroscopy (IMPS/IMVS). IMPS is a form of impedance spectroscopy that records the phase shift in photocurrent in relation to a modulated light intensity.[42] Likewise, IMVS probes the photovoltage response in relation to the light intensity modulation.[43] The implementation of IMVS in PEC systems is far less than that of IMPS. In fact, IMVS is widely used for solar cells.[44,45] Recently, a few groups have used IMVS to measure the electron lifetime of photoelectrodes. However, the measurement is performed under open circuit conditions, which correspond exclusively to the bulk electron lifetime

without considering the influence of interfacial charge transfer.[46,47] Hence, we skip IMVS and focus on IMPS in this part.

Figure 3a shows a typical scheme of the setup for IMPS measurements, where the modulated illumination is realized by a light emitting diode (LED) in cooperation with a frequency response analyser (FRA). A beam splitter splits the LED light into two beams, one of which goes straightforward as the light source for the PEC cell, and the other arrives at a high-speed Si photodiode that senses the light intensity. The signal output of the FRA is used to create the sinusoidal modulation of light intensity, with a small amplitude superimposed onto a constant background illumination.[48]

Thanks to the pioneering work by Peter and coworkers, the IMPS technique has been widely applied in the PEC field.[42,49] This technique offers a convenient way to measure the rate constants k_{ct} and k_{rec} of photoelectrodes. Due to the small amplitude of modulation, it is assumed that the change of light intensity alters only the concentration of surface carriers but not the band bending degree in semiconductors, making it possible to extract interfacial carrier dynamics from the photocurrent changing response.[47] The IMPS response as a function of angular frequency (ω) can be described by the normalized transfer function:

$$\frac{j_{photo}}{j_h} = \frac{k_{ct} + i\omega}{k_{ct} + k_{rec} + i\omega} \quad (i^2 = -1) \tag{3}$$

where j_{photo} stands for the measured photocurrent and j_h represents the hole current that flows into the photoelectrode surface.[42,50] The equation corresponds to the normalized Nyquist plots (Figure 3b) in the complex plane, with the real and imaginary parts as follow:

$$Re(\frac{j_{photo}}{j_h}) = \frac{k_{ct}(k_{ct} + k_{rec}) + \omega^2}{(k_{ct} + k_{rec})^2 + \omega^2} \tag{4}$$

$$Im(\frac{j_{photo}}{j_h}) = \frac{k_{rec}\omega}{(k_{ct} + k_{rec})^2 + \omega^2} \tag{5}$$

At high frequency intercept, the real part equals 1, since the measured photocurrent equals the hole current due to fast modulation which freezes out the surface recombination.[51] At low frequency intercept, the real part corresponds to the fraction of hole current that undergoes interfacial charge transfer, which is defined as the interfacial charge transfer efficiency (η_{ct}):[52]

$$\eta_{ct} = \frac{k_{ct}}{k_{ct} + k_{rec}} \tag{6}$$

The imaginary part reaches maximum at ω_{max}:

$$\omega_{max} = k_{ct} + k_{rec} \tag{7}$$

Hence, k_{ct} and k_{rec} can be calculated through the above equations, and the corresponding key data points are labelled in Figure 3b. The validity of the IMPS data can be examined by the Gärtner model.[47] The theoretical hole current flowing into the photoelectrode surface is given by the Gärtner equation:[53,54]

$$j_h = -q\phi(1 - \frac{e^{-\alpha W}}{1 + \alpha L_p}) \tag{8}$$

where q, ϕ, α, and L_p stand for the elementary charge, the light intensity, the absorption coefficient at a certain wavelength, and the hole diffusion distance, respectively, and W is the width of charge space layer which changes with the applied potential as follow:

$$\mathrm{W} = [\frac{2\varepsilon\varepsilon_0(V_{app} - V_{fb})}{N_D}]^{1/2} \tag{9}$$

where ε, V_{app}, V_{fb}, and N_D represent the dielectric constant, the applied potential, the flat band potential, and the carrier concentration of the semiconductor. ε_0 is vacuum permittivity. The illuminated J-V curve can be predicted by multiplying the Gartner hole current with the η_{ct} obtained from IMPS, and the IMPS data can be confirmed valid when the predicted J-V curve matches well with the measured one.[47]

Using this method, k_{ct} of representative photoanodes such as $BiVO_4$ and α-Fe_2O_3 have been reported within a magnitude of 10 s^{-1} to 100 s^{-1}.[47,48] Guijarro and coworkers interrogated the Cu_2FeO_4 photoanode, suggesting that the slow rate of charge transfer (k_{ct}~5 s^{-1}) plays a critical role in the Fermi level pining.[46] They also found that the effectiveness of water oxidation is strongly limited by the competing surface recombination, which is inferred by the onset of photocurrent at the potential region where k_{ct} exceeds k_{rec}.[46] Wang's group reveals that the $NiFeO_x$ OER catalyst improves the PEC activity of hematite through a passivation effect rather than a catalytic effect, which is evidenced by the decreased k_{rec} and the preserved k_{ct} after the catalyst modification (Figure 3c).[47] Furthermore, they also found that the heterogenized molecular Ir catalyst can speed up the charge transfer on hematite photoanode but leave the surface charge recombination unchanged, whereas the heterogeneous IrO_x realizes simultaneous increase of k_{ct} and decrease of k_{rec}.[55] Similar analysis was also applied on $BiVO_4$, where the photocurrent can be improved by the surface-passivating CoPi catalyst, while the non-passivating RuO_x catalyst renders no improvement.[48]

Despite the abundant findings coming from the rate constant calculation by IMPS, the reliability of this calculation is questioned by some researchers especially when ECs are involved in the PEC system.[56,57] The original model was developed for a simple system without ECs and involves only two kinetic processes, whereas the ECs can induce more complicated processes possibly including all the pathways of forward and reverse electron and hole transfer between the semiconductor, electrocatalyst, surface states, and electrolyte. Therefore, Grave *et al* suggested an analysis method which yields the magnitude of hole current and surface recombination current without a priori assumption of mechanistic model, and thus it should be more applicable for the electrocatalyst integrated photoelectrodes as compared to the rate constant analysis.[57] As shown in Figure 3d, $Y_{pc}^{+}(0)$, $Y_{pc}^{-}(0)$, and the difference between $Y_{pc}^{+}(0)$ and $Y_{pc}^{-}(0)$ are supposed to account for hole current, surface recombination current, and the interfacial hole transfer-determined photocurrent, respectively. Using α-Fe_2O_3/$NiFeO_x$ as the study model, their group revealed that the role of electrocatalysts in PEC system is influenced by the dopant in SCs. Sn-doped α-Fe_2O_3 shows stronger surface charge recombination than Zn-doped α-Fe_2O_3 (Figure 3f and 3f).[57] Since Sn acts as a donor while Zn acts as an

acceptor when doping in α-Fe_2O_3, the electron concentration in the Sn-doped

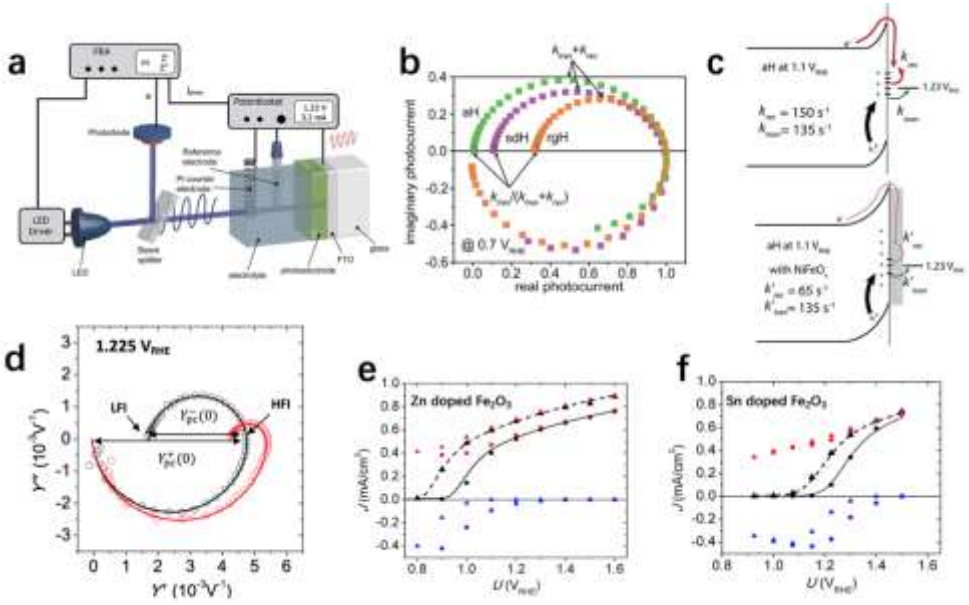

Figure 3. (a) Schematic diagram of the IMPS setup. Reproduced with permission from ref. [48]. Copyright 2017 The Royal Society of Chemistry. (b) Normalized IMPS-Nyquist plots of three hematite photoanodes, with labels of the critical data points for rate constant calculation. (c) k_{ct} and k_{rec} of $NiFeO_x$ modified and bare hematite photoanodes measured by IMPS. Reproduced with permission from ref. [47]. Copyright 2016 The Royal Society of Chemistry. (d) IMPS-Nyquist plots of 1% Sn-doped hematite before (black circles) and after (red circles) $FeNiO_x$ overlayer deposition, with labels of the indicators of hole current ($Y_{pc}^{+}(0)$) and surface recombination current ($Y_{pc}^{-}(0)$). Results of the IMPS analysis showing hole current (red), photocurrent (black), and surface recombination current (blue) as a function of the applied potential for (e) 1% Sn- and (f) 1% Zn-doped hematite photoanodes. Circles and triangles stand for photoanodes before and after the $FeNiO_x$ overlayer deposition, respectively. Full and dashed lines represent photocurrent voltammograms measured before and after the $FeNiO_x$ overlayer deposition, respectively. Reproduced with permission from ref. [57]. Copyright 2018 American Chemical Society.

α-Fe_2O_3 is higher than that in Zn-doped α-Fe_2O_3. The higher electron concentration in the SC results in thinner space charge layer, giving rise to a higher probability of electron tunnelling to the SC surface, thus leading to the stronger interfacial charge recombination between SC electrons and EC holes.

2.2 Open circuit potential (OCP) technique.

OCP technique measures the potential of working electrodes under open circuit condition where zero current is passed. It is utilized to investigate the interfacial thermodynamics in PEC systems. In dark condition, Fermi level of a photoanode in equilibrium with the electrolyte can be measured as OCP (Figure 4a).[58] Under illumination, quasi-fermi levels of electrons and holes are used to describe the interfacial thermodynamics due to the photogenerated carriers. The quasi Fermi level of holes is responsible for photoanode-electrolyte equilibrium, whereas the quasi Fermi level of electrons can be detected as OCP under illumination (Figure 4b). Therefore, the photovoltage (V_{ph}) can be recorded as the difference between OCP in the dark and under illumination (Figure 4b).[58-60]

Wang's group carried out a series of studies to explore the role of ECs and other overlayer modifications in PEC systems.[61-63] They scrutinized the PEC and OCP responses of hematite photoanodes with and without $NiFeO_x$ coating, finding that the cathodic shift of the onset potential (Figure 4c) has quite close value with the V_{ph} enhancement (Figure 4d). Thus, they attributed the PEC performance improvement induced by $NiFeO_x$ dominantly to the thermodynamic factor.[64] Similar V_{ph} improvement can be realized by atomic layer deposition (ALD) grown overlayers such as TiO_2,[11,65] Al_2O_3,[12] and Ta_2O_5,[66] where the ultrathin and compact overlayers can passivate the surface states of SCs and alleviate Fermi level pining. The surface passivation effect can also be achieved by curing the surface defects of SCs using ultraviolet light treatment,[67] or reducing the surface disorders using a hydrothermal regrowth strategy.[68] However, some overlayers can aggravate Fermi level pining when interface with semiconductors. It was reported that coating the active OER catalyst MnO_x on hematite photoanode surprisingly decreased the PEC performance.[62] The anodically shifted photocurrent onset can be attributed to the reduced V_{ph} that results from the Fermi level pining effect due to MnO_x introduction.[62]

Despite the convenient measurement of V_{ph} by the OCP technique, it is cautioned that the V_{ph} measured at open circuit may deviate from the V_{ph} under the operating PEC condition since the kinetic overpotential should be considered in the later condition.[58] The V_{ph} under operating PEC conditions can be measured by more advanced techniques which will be introduced in section 2.4.

2.3 Cyclic voltammetry (CV) and chopped-light chronoamperometry (CA)

CV and chopped-light CA are two easily accessible techniques to measure the charge accumulation at the electrode-electrolyte interface during PEC process, which can offer further

information about interfacial charge transfer and surface states of SCs.

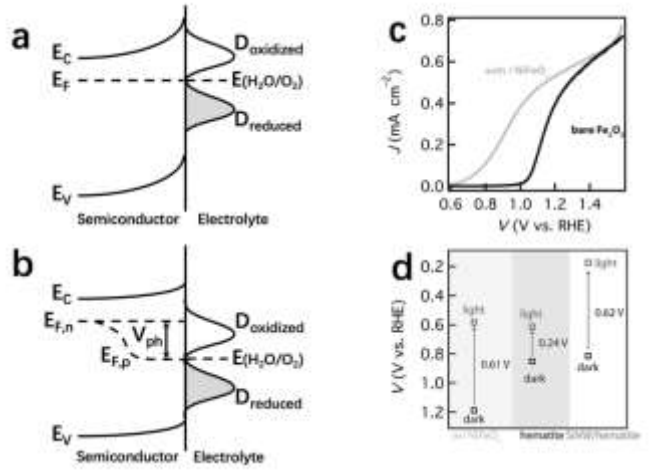

Figure 4. Band diagrams of a n-type semiconductor in contact with the solution in (a) absence and (b) presence of illumination. (c) Photocurrent density–voltage plot showing the substantial cathodic shift (up to 0.38 V) observed upon the surface modification of hematite with $NiFeO_x$. (d) Graph showing the significant difference observed between the OCP measured photovoltages generated by bare hematite and hematite decorated with $NiFeO_x$. Reproduced with permission from ref. [64]. Copyright 2013 Wiley-VCH.

Hole accumulation at the photoanode surface is inevitable during PEC water splitting due to the slow water oxidation kinetics, which can be manifested by comparing the difference of electrochemical signals from water oxidation and those from hole sacrificial agents with fast oxidation kinetics such as H_2O_2 (Figure 5a-5c).[69-71] The CV plots within the water oxidation potential range display a cathodic capacitive peak resulting from the discharging of surface accumulated holes (Figure 5a), which are not observed when adding H_2O_2 (Figure 5b).[70] Besides, the CV technique can also be used to characterize the surface states of SCs, which is realized through photoelectrochemically oxidizing the surface states at a positive potential followed by measuring a cathodic scan in dark to reduce the initially oxidized surface states, and thus the resulted negative capacitive peak can be a probe of surface states.[14,24,72] By using the CV technique, Hamann *et al* detected two distinct surface states on hematite as interfacial charge recombination centre and water oxidation intermediates, respectively.[14]

In a chopped-light CA measurement, current spikes are observed during water oxidation but they disappear when adding H_2O_2 (Figure 5c).[69] The negative current spikes upon turning light off represent the electron flow from the SC conduction band, which undergoes recombination with the surface holes. Therefore, the amount of surface accumulated holes can be determined by integrating the current *vs.* time plots within the negative spike ranges.[24] The chopped-light CA technique are widely applied in detecting the hole storage behaviour of many transition metal oxide and (oxy)hydroxide overlayers in PEC systems, where the photogenerated holes are spatially extracted away from the photo-absorber to the hole storage layers thus to alleviate photocorrosion.[73,74] Moreover, by quantitatively analysing the change of interfacial charge accumulation, information about interfacial charge transfer in multilayer photoelectrodes can be obtained.[75]

By using CV and chopped-light chronoamperometry techniques, Cui *et al* investigated the interfacial charge transfer in a multilayer photoanode.[75] They fabricated atomically dispersed Ir-sites on the hematite photoanode by using a metal oxide (MO_x) interlayer. Under PEC conditions, the positively charged MO_x electrostatically absorbs the soluble monomeric $[Ir(OH)_6]^{2-}$ onto the photoanode surface, where it also acts as a bridge for hole transfer from the hematite surface to the single iridium centre, accelerating the OER kinetics (Figure 5d). There is no significant charge transfer between hematite and Ir-anion in the absence of NiO_x, whereas efficient hole transfer from hematite to the Ir centres occurs through the NiO_x interlayer, which is evidenced by the variation of CV peaks (Figure 5e). The quantity of hole accumulation at the photoanode surface was measured by the chopped-light chronoamperometry technique. Compared to the Ir-absent hematite-NiO_x photoanode, adding $[Ir(OH)_6]^{2-}$ reduced the hole accumulation at the photoanode surface (Figure 5f, grey square), indicating the efficient hole transfer from the interlayer to the highly active Ir-site which accelerates the hole consumption for OER. The authors further compared several kinds of MO_x interlayers, finding the consistent relationship between the hole accumulation capacity of MO_x and the enhanced PEC performance caused by the $[Ir(OH)_6]^{2-}$, where the NiO_x exhibits the highest hole accumulation capacity in company with the largest enhancement of photocurrent density upon adding $[Ir(OH)_6]^{2-}$ (Figure 5f).[75] Through similar analysis, the critical role of interlayer as a hole transfer bridge was also clarified in a hematite/$Ni(OH)_2$/IrO_2 photoanode.[76]

The chopped-light CA technique has been extensively used in PEC studies nowadays, as it can be easily accessible and time-saving. However, this technique can not accurately quantify the hole accumulation at a high applied bias. The quantification of hole accumulation from the negative spikes is based on the assumption that all the surface holes contribute to the recombination current upon turning light off, but this assumption is only applicable under low bias where water oxidation has not been triggered. With increasing applied bias, the surface hole-back electron recombination is gradually inhibited and even cut off due to the widened space charge layer, and thus surface holes are more prone to participate in water oxidation instead of charge recombination. This is consistent with the injection efficiencies which approach unit under sufficiently high potentials, where the negative spikes gradually decrease and eventually disappear. Under this condition, hole accumulation cannot be probed by the chopped-light CA technique, and more advanced techniques are needed which will be introduced in section 3.1.3.

2.4 Due-working-electrode (DWE) technique

DWE is a newly emerged technique that is first proposed by Boettcher's group in 2014. It is specially developed to study the SC/EC interfaces during PEC reaction.[9] It allows for direct in situ electrochemical measurement and control of the potential and

the current of the EC in the SC/EC composite photoelectrode, which are impossible by using the conventional techniques

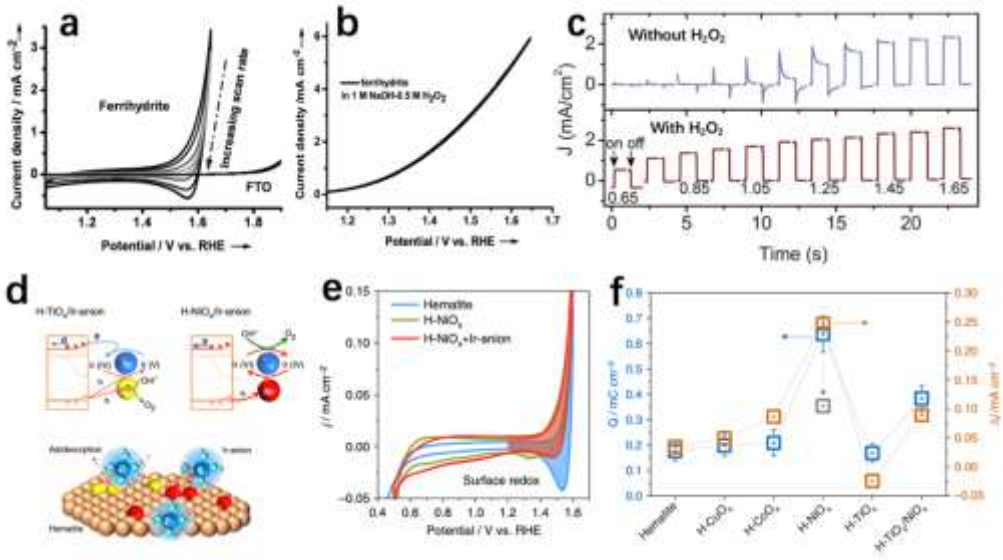

Figure 5. Cyclic voltammograms for ferrihydrite in 1 M NaOH electrolyte (a) without and (b) with 0.5 M H_2O_2 under scan rate of 100 mV s^{-1} with 3 cycles. Reproduced with permission from ref. [70]. Copyright 2014 Wiley-VCH. (c) Chopped light chronoamperometry measurements of hematite electrodes in 1 M NaOH without or without 0.5 M H_2O_2. Reproduced with permission from ref. [69]. Copyright 2011 The Royal Society of Chemistry. (d) Proposed reaction paths explaining the different roles of TiO_x and NiO_x for the PEC-OER. (e) Cyclic voltammetry at 50 mV s^{-1} on pristine, NiO_x coated, and NiO_x/Ir-anion modified hematite in 1.0 M NaOH in the dark. (f) The correlation between the hole accumulation capacity of hematite-MO_x before the addition of Ir-anion and the activity difference Δj after the introduction of 1.0 μM Ir-anion relative to the Ir-anion-free electrolytes. The grey arrow shows the decreased capacity of hematite-NiO_x from 0.64 to 0.35 mC cm^{-2} (grey square) after the introduction of Ir-anion to the electrolyte. Error bars represent the standard deviation. Reproduced with permission from ref. [75]. Copyright 2017 Springer Nature.

introduced above. The DWE technique is based on two working electrodes in independent contact with SC and EC, respectively.[21] The key challenge of this technique is to construct a workable second electrode which has a good contact with the EC but avoids shorting to the underlying SC.[56] A bipotentiostat is implemented in the DWE-PEC experiment to allow simultaneous control of the two working electrodes.[21] The data collection and interpretation of DWE technique are straightforward without much assumptions and models. The measurement relies only on the equilibration of electrochemical potential between the second working electrode and the feature of interest.

2.4.1 Thin Au film as the second working electrode. The fundamentals of the thin Au film-based DWE photoelectrochemistry are illustrated in Figure 6a. The electrocatalyst is deposited on the front side of the SC, while an ohmic contact is made to the back as the first working electrode (WE1). The electrocatalyst is coated with a thin layer of Au (~10 nm) by vacuum evaporation to create the second working electrode (WE2). The Au film should be porous, ensuring continuous conductivity, electrolyte permeability, as well as optical transmission.[21]

Significant insights of the SC/EC interfaces have been provided by Boettcher and coworkers using the DWE technique. They recorded the steady state potential of the electrocatalysts (V_{cat}) when stepping the semiconductor electrode potential (V_{sem}) for $Ni(OH)_2$ or IrO_x modified TiO_2 photoanodes under PEC conditions.[9] The increasing V_{cat} with V_{sem} (Figure 6b) is a direct proof of positive charge accumulation in the electrocatalyst layers which results in a decreased electrocatalyst Fermi level. The rapid change of V_{cat} with V_{sem} for $Ni(OH)_2$ coated TiO_2 and the linear change of V_{cat} with V_{sem} for IrO_x coated TiO_2 can be explained by the different ion-permeability of the two ECs. the ion-permeable $Ni(OH)_2$ form adaptive junctions with the SC, where the effective Schottky barrier height changes in operando with the bias-dependent oxidation level of the EC. In contrast, the ion-impermeable IrO_x form buried junctions with the SC, yielding a constant barrier height independent of applied bias. The DWE technique was also used to track whether the photogenerated holes in the SC travel through the EC or directly go into the solution (Figure 6c). The illuminated CV plot measured at WE2 shows a negative shift compared to the dark CV plot by ~0.2 mA cm^{-2}, which equals the photocurrent measured at WE1, demonstrating that photogenerated holes are collected by the EC layer rather than directly drive water oxidation on the SC surface.[9] The group further studied the α-Fe_2O_3/$Ni_{0.8}Fe_{0.2}O_x$ photoanode, finding that the photovoltage across α-Fe_2O_3/$Ni_{0.8}Fe_{0.2}O_x$ substantially decreases with the operative oxidation and conductivity switch of $Ni_{0.8}Fe_{0.2}O_x$ (Figure 6d), since the SC/EC junction photovoltage is determined by the balance of electron and hole transfer to the EC.[77] Moreover, they studied the Ni-protected Si photoanode and found that the photovoltage can be increased by developing a spatially inhomogeneous buried junction, which is realized by thinning the protection layer to facilitate solution permeation to the n-Si/Ni interface.[78,79] The increased photovoltage can be explained by the "pinch-off" effect, where charge depletion in the high barrier regions can spill into the low

barrier regions thus to increase the local built-in potential.[78,80] Furthermore, they studied how the semiconductor morphology

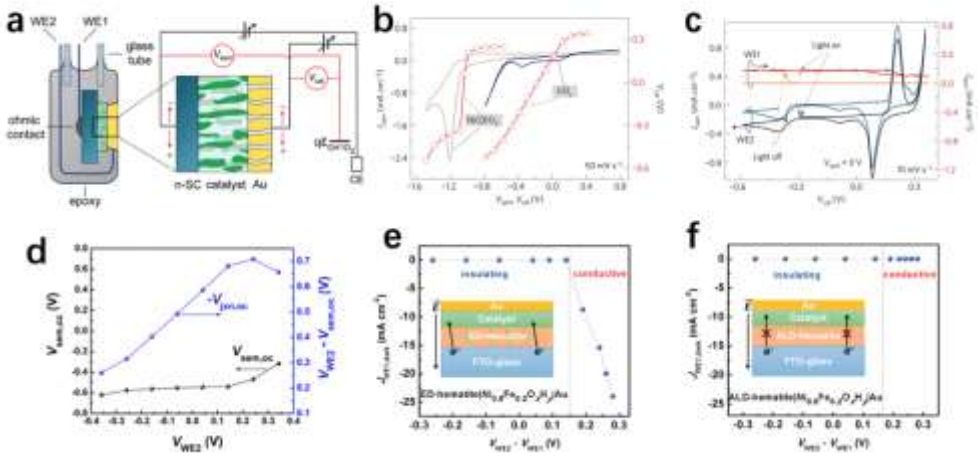

Figure 6. (a) Dual-working-electrode photoelectrochemistry. Semiconductor and electrocatalyst potentials are independently measured/varied relative to the reversible oxygen potential, ε_{O_2/OH^-}. Reproduced with permission from ref. [21]. Copyright 2016 American Chemical Society. (b) Steady-state electrocatalyst potential (V_{cat}) as a function of the TiO_2 potential (V_{sem}) under illumination. Each V_{cat} data point was collected after holding V_{sem} for 180 s. Illuminated voltammograms collected through the TiO_2 electrode (WE1) are shown for reference. In both cases, V_{cat} reaches a constant value for sufficiently positive V_{sem}, consistent with the requirement for continuity of the interfacial and OER currents, and the activity of the catalysts. (c) Voltammetry of the $Ni(OH)_2$ electrocatalyst (through the porous Au WE2) while V_{sem} was held at 0 V *vs.* ε_{O_2/OH^-} in the dark (blue) and under 1 sun illumination (black). The blue (light) and orange (dark) curves show J_{sem} at the TiO_2 WE1 during the scan. The green arrows indicate the scan direction. Reproduced with permission from ref. 9. Copyright 2014 Springer Nature. (d) The $V_{sem,oc}$ of α-Fe_2O_3 and the $V_{jxn,oc}$ for α-Fe_2O_3/$Ni_{0.8}Fe_{0.2}O_x$ both as a function of V_{WE2} (V_{cat}) under illumination. Reproduced with permission from ref. [77]. Copy right 2017 American Chemical Society. Current density passing from Au through (e) $Ni_{0.8}Fe_{0.2}O_xH_y$-catalyzed electrodeposited hematite (porous) and (f) $Ni_{0.8}Fe_{0.2}O_xH_y$-catalyzed ALD-hematite (uniform and compact) to the FTO substrate when V_{WE1} is held at 0 V vs ε_{O_2/OH^-} and V_{WE2} is set at various potentials. Reproduced with permission from ref. [81]. Copy right 2018 American Chemical Society.

and electrocatalyst conductivity influence the interfacial charge behaviour in an α-Fe_2O_3/$Ni_{0.8}Fe_{0.2}O_xH_y$ system.[81] The conductive $Ni_{0.8}Fe_{0.2}O_xH_y$ can induce substantial "shunt" recombination current once it simultaneously contacts both the semiconductor and the underlying conducting substrate (Figure 6e), thus damaging the PEC performance. This recombination pathway can be locked by constructing pinhole-free semiconductors, where negligible "shunt" recombination current can be observed even when the catalyst is oxidized and conductive (Figure 6f). Other solutions are suggested including selectively depositing the EC on the SC surface, or inserting an insulate oxide layer between SC and EC.[81]

In spite of the exciting works mentioned above, challenges still remain for the DWE technique. When DWE is applied on nanostructured SCs coupled with nonuniform EC coverage, a thin Au top contact may short to the underlying SC, hindering the independent monitoring and controlling of SC and EC.[56] Besides, the thin Au film has difficulty to simultaneously maintain a good interconnection and electrolyte permeability for rather rough photoelectrode surfaces. To overcome these challenges, the WE2 with new a material and structure should be developed.

2.4.2 Potential-sensing electrochemical atomic force microscopy (PS-ECAFM). Instead of using the thin film Au as the second electrode for macroscopic measurement, PS-ECAFM uses nanoelectrode atomic force microscopy (AFM) probes to realize a spatial resolution in nanoscale.[82,83] The conductive AFM probes are entirely coated by a thin insulating layer except for the exposed tip (Figure 7a). The tip scans the photoelectrode with incomplete EC coverage to distinguish the bare SE surface from the electrocatalyst-coated locations.[56]

The group has studied α-Fe_2O_3/CoPi and $BiVO_4$/CoPi by PS-ECAFM, where they draw conclusions consistent with those by using Au-based DWE. They compared the electrocatalyst potentials (V_{tip}) driving a certain OER current in α-Fe_2O_3/CoPi and ITO/CoPi systems with the same amount of CoPi (Figure 7b).[83] For a given current density, CoPi loaded on α-Fe_2O_3 under the PEC condition shows nearly identical potentials to those measured for CoPi-ITO in dark, indicating that photogenerated holes in α-Fe_2O_3 transfer to the electrocatalyst layer to oxidize CoPi until it reaches a potential necessary to mediate a water oxidation current equal to the steady-state photocurrent (Figure 7b).[83] Generally similar behaviour was also observed for CoPi loaded on a $BiVO_4$ photoanode.[84] The combined data evidences that CoPi harvests photogenerated holes from SCs and catalyses OER instead of acting as a spectator during the PEC process.[83]

Furthermore, the nanoscale resolution of electrochemical signals under PEC conditions, which is the unique advantage of PS-ECAFM, is utilized to verify the pinch-off effect in an n-Si/Ni/NiOOH photoanode.[85] The authors performed photovoltage measurements of the nanoscale Si/Ni/NiOOH junctions by selectively landing the AFM probe on individual Ni/NiOOH islands (Figure 7c). The results are displayed as a topographic map as shown in Figure 7d, where the photovoltages at smaller islands are higher than those at larger islands. The size dependence can be explained by the pinch-off

effect, where the oxidized NiOOH on Si produces high-barrier regions surrounding the low-barrier regions of Si/Ni interfaces

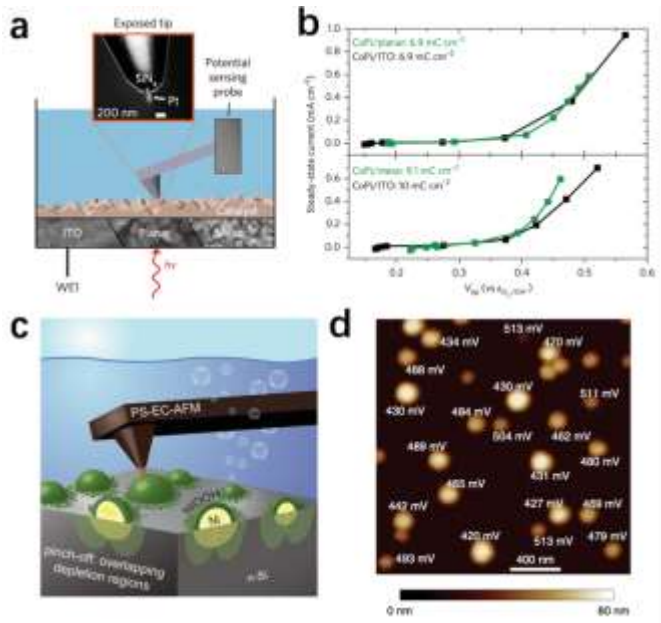

Figure 7. (a) The PS-ECAFM setup with the cantilever, fully electrically insulated except for the exposed nanotip, serving as a potential probe. The inset is an electron micrograph of the AFM tip used. The blue colour represents electrolyte. (b) CoPi surface potential measurements at given current densities. The fact that the curves for the conducting ITO substrates overlay those of the semiconductor photoelectrode substrates indicates that the catalyst is behaving in the same fashion in both cases, independent of whether the holes originate from the ITO or are photogenerated in the haematite. Reproduced with permission from ref. [83]. Copy right 2017 Springer Nature. (c) Schematic illustration of pinch-off effect evidenced by sensing the individual Ni/NiOOH islands on Si by PS-ECAFM. (d) Operando photovoltages collected at different nanoscale regions of the n-Si/Ni/NiOOH photoanode. Reproduced with permission from ref. [85]. Copyright 2019 Springer Nature.

due to the higher work function of NiOOH than that of metallic Ni. Therefore, the pinched-off junction exhibits higher effective barrier height of Si/Ni interfaces and higher interfacial selectivity for holes as compared to the non-pinched off analogues.[85]

Similar to PS-ECAFM, photoconductive AFM (pc-AFM) was performed to enable nanoscale imaging of charge carrier transport in photoanodes.[86] Photocurrent from grain boundaries, facet planes, and facet boundaries can be distinguished using pc-AFM. In a nanostructured $BiVO_4$ photoanode, no additional recombination centre was observed at grain boundaries, indicating the high defect tolerance. Moreover, through the complementary pc-AFM and macroscopic PEC measurement, the roles of different overlayers on $BiVO_4$ photoanode were revealed, where $(NiFe)O_x$ acted as the catalytic component and $(CoFeCe)O_x$ had the function of hole capture.[87] These findings facilitate the interface optimization in multi-component photoelectrodes.

The applicability and weakness of all the introduced electrochemical techniques are briefly summarized in Table 2, which may instruct the selection of techniques and evaluation of the data reliability. Although the conventional electrochemical techniques have supported plenty of mechanistic PEC interface studies, innovation of the technique development is still strongly encouraged towards more powerful functions and wider applications.

3. Optical spectroscopic techniques

Optical spectroscopic methods can provide useful information on the reaction intermediates and carrier dynamics, which are pivotal for revealing the reaction mechanism and interfacial charge behaviour during PEC water splitting. Significant progress has been made in implementing optical spectroscopic methods in PEC systems, including both steady-state and transient spectroscopic techniques.

3.1 Steady-state optical spectroscopy

Steady-state optical spectroscopy is generally applied to study PEC reaction intermediates and pathways. The reaction intermediates during PEC water oxidation had been suggested to be some surface-bond higher valent species by a series of electrochemical studies through the hole accumulation phenomenon at photoanode surface, but the chemical nature of the intermediate species was blurred.[24,88,89] To address the issues, optical spectroscopic methods play a key role. To obtain the optical signals at real PEC conditions, two beams of light are required, one of which act as the illumination source to drive the PEC reaction, and the other as the probe of optical response.[71,90] The PEC illumination light should be prevented from entering the optical detector by using filters or modulating the light path.[90,91] The measurement can be conducted as a function of applied bias, illumination intensity, or electrolyte environment, guiding detailed PEC mechanistic study.

3.1.1 Spectroelectrochemistry. Spectroelectrochemical experiments can be performed by incorporating a quartz cell into an ultraviolet (UV)-visible spectrometer, collecting the absorption spectra of photoelectrodes as a function of applied bias.[92] Without PEC illumination, the featured absorption peaks increasing with positive potentials were observed at 580 nm for hematite and 470 nm for $BiVO_4$, both of which could be related to the bias-dependent space charge layer width in semiconductors.[92,93] Furthermore, spectroelectrochemical experiments can be conducted under illumination, where a monochromatic laser beam is added as the constant illumination source, and a long pass filter should be equipped to prevent the laser beam from going into the UV-visible detector.[90] Spectroelectrochemical experiment under PEC condition were performed by Klahr *et al*. to study the nature of surface oxidized species on hematite photoanodes.[90] They observed the absorption difference spectra for various applied potentials and found a peak growing at 572 nm with increasing anodic potentials. This peak was reduced by an alumina coating, confirming that it results from surface species of hematite rather than bulk trap states.[90] The absorption peak at 572 nm shows a linear relationship with surface charge calculated from CV measurements, and a striking similarity with the absorption peak of isolated molecular Fe(V)B*(=O) species. Hence, it was

tentatively assigned to high valent Fe=O groups that accumulate at hematite surface for water oxidation.[90,94] Besides,

Table 2. A summary and comparison of electrochemical techniques for interface study in PEC systems.

Technique	Outputs	Weaknesses	Ref.
PEIS	Identification of charge behaviour at different interfaces Rate constant calculation	Fitting models rely on prior assumptions.	26,39
IMPS	Rate constant calculation Surface hole current and recombination current measurement	Rate constant calculation relies on prior assumptions.	55,57
OCP	Photovoltage measurement	V_{ph} measured at open circuit may deviate from the V_{ph} under the operating PEC condition.	58,64
CV	Observation of interfacial charge accumulation	Cannot quantify the charge accumulation.	75
Chopped-light CA	Quantification of interfacial charge accumulation	Limited application only for low-injection efficiency conditions.	70
Au-based DWE	In situ macroscopic measurement/control of the potential and the current of the EC in the SC/EC composite photoelectrode	Au top contact may short to the underlying SC when EC is ununiform.	9,56
PS-ECAFM	In situ measurement/control of the potential and the current of the EC in the SC/EC composite photoelectrode with nanoscale spatial resolution	Complicated setups	83,85

Irie *et al.* investigated the intermediate species on hematite photoanode in a wide pH range by in situ spectroelectrochemical measurement.[95] They concluded that the pH-dependent photocurrent onset can be ascribed to two reaction mechanisms switching at approximately pH 10.[95] Consistently, a theoretical simulation also suggested the electrolyte pH-dependent surface states and interfacial charge transfer mechanisms of hematite photoanodes.[96] Although operando spectroelectrochemistry can provide clues for the water oxidation intermediates, it was usually performed in the UV-visible region which is not powerful for chemical bond identification.

3.1.2 Attenuated total reflectance infrared (ATR-IR) spectroscopy. In situ ATR-IR spectroscopy was first implemented in PEC study by Hamman's group, achieving the first exact identification of the PEC water oxidation intermediate on hematite photoanode.[91] This technique has the superiority including limited detecting region near the electrode-electrolyte interface and high sensitivity for low-concentration species.

The measurement setup was developed by sandwiching the electrolyte within a micrometer distance between a hematite photoanode and a ZnSe ATR element (Figure 8a). An LED ultraviolet flashlight is used as the light source for PEC reaction, which illuminates the photoanode from backside. The incident IR beam reflects at the ZnSe-electrolyte interface, forming evanescent wave which penetrates a limited path length of typically 0.5~2 micrometres into the electrolyte, thus the problem of competitive IR absorption by water can be alleviated.[97,98] Besides, IR light undergoes multiple internal reflections in the ZnSe single crystal to enhance its interaction with the substance in electrolyte, thus addressing the challenge of probing the low-concentration intermediate species on the photoanode surface.[98] All experiments were performed in D_2O to ensure a sufficient IR transmittance. The identification of the PEC water oxidation intermediate includes three steps.[91] First, the IR spectra under varied applied potentials were collected, and a prominent absorption peak at 898 cm^{-1} was observed at potentials anodic to the onset potential of OER current, whereas the peak is absent at potentials that render no OER current (Figure 8b). Second, when introducing KI as a hole scavenger into the electrolyte, no spectral feature was observed. Therefore, the absorption peak at 898 cm^{-1} can be ascribed to the reaction intermediate that is unique to the OER reaction. This peak can be assigned to either Fe=O or Fe-O-OH groups, thus the third step is to explore the isotopic effect on the IR spectra to further differentiate between the two species. The 1:1 ratio mixture of $D_2{}^{16}O$/ $D_2{}^{18}O$ results in two equally weighted peaks at 898 and 857 cm^{-1} (Figure 8c) corresponding to $Fe^{IV}=^{16}O$ and $Fe^{IV}=^{18}O$ groups, respectively, thus eliminating the possibility of Fe–O–OH groups which would produce three different stretching modes. Therefore, the chemical identity of the PEC water oxidation intermediates on hematite can be confirmed as $Fe^{IV}=O$.[91]

ATR-IR spectroscopy was further used to observe the reaction intermediates in different electrolyte environment by Zhang *et al*, who reported a pH-dependent interfacial charge transfer pathway.[99] The rate-determining step for water oxidation on hematite photoanode, namely O-O bond formation, undergoes distinct pathways in different pH regions. They observed an absorption band of water oxidation intermediates at 1100 cm^{-1}, and it was assigned to a surface superoxide species through a further investigation of the isotopic effect on the absorption spectra. However, this absorption band at 1100 cm^{-1} gradually decreases from pH 8 to pH 10, and completely disappears at pH 11 (Figure 8d). Meanwhile, they performed a rate law study through PEIS measurements and found that interfacial hole transfer changes from a first order reaction to a second order reaction as pH increases (Figure 8e). Water oxidation intermediates and the reaction orders display the consistent pH-dependences, indicating the transition of reaction pathway way with increasing pH (Figure 8f). In near neutral pH region, O-O bond forms through the nucleophilic attack of water to surface trapped holes (WNA mechanism). At high pH extremes, the prevailing mechanism is the coupling of the neighbouring metal-oxo species (I2M mechanism).[99]

3.1.3 Photoinduced absorption (PIA) spectroscopy. PIA spectroscopy was first applied in PEC studies by Durrant's group, aiming at quantifying the hole concentration on photoanode surface under PEC working conditions.[71] It measures the optical absorption of illuminated photoelectrodes as a function of illumination intensity, and the PIA signal is recorded as the absorption difference between illuminated- and unilluminated- photoelectrodes. The illumination light should be attenuated in the front of the optical detector by filters. Different from the electrochemical techniques which primarily monitor the electron signals, PIA enables researchers to directly monitor the presence of photogenerated holes by the observation of their optical absorption. This is especially important to photoanodes, where the photogenerated holes drive the key function of water oxidation.[100]

A model study of quantifying the photoanode surface hole concentration by using PIA was carried out on hematite, enabling a rate law analysis towards a deep understanding on the PEC water oxidation kinetics.[71] A single-wavelength light of 650 nm was used as the absorption probe, since it is an indicator of the surface photoholes on hematite.[101] The analysis was conducted by two steps. First, the hematite photoanode was kept at a constant potential just negative to the photocurrent onset, where the PIA signal and the chopped light CA curves are simultaneously measured as a function of illumination intensity. Thereafter, the surface hole concentration can be calculated by the negative current spikes and quantitatively correlated to the PIA signals. Based on this quantitative correlation, the surface hole concentration can be extracted from the PIA intensity at any potentials even if the current spikes disappear. Second, the hematite photoanode was kept at a sufficiently positive potential where the surface holes are completely utilized for surface reaction, and thus the rate law of PEC water oxidation can be constructed by quantifying the correlation between surface hole concentration and photocurrent density (Figure 9a and 9b). The result indicates that increasing surface hole concentration can turn the first order reaction to third order reaction (Figure 9c).[71] Beside hematite, $BiVO_4$ photoanodes also display a transition of water oxidation reaction order from 1 to 3 with increasing surface hole concentration.[102] Moreover, the rate law analysis was also carried out on TiO_2, where a pH-dependent reaction order was observed.[103]

The hole concentration-dependent reaction kinesics in PEC system is unique for water oxidation. For hole scavengers like

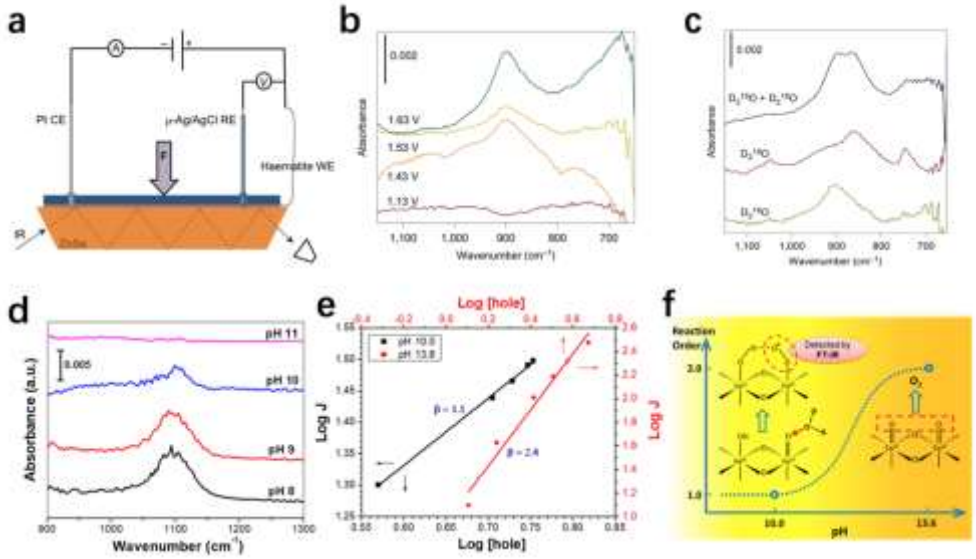

Figure 8. (a) Schematic of the set-up used for operando PEC infrared (IR) measurements depicting the hematite working electrode (WE), platinum counter electrode (CE), Ag/AgCl reference electrode (RE) and ZnSe ATR crystal. A thin layer of electrolyte was introduced between the hematite WE and the ATR crystal. (b) Infrared spectra of hematite scanned at constant applied potentials, from 1.13 to 1.63 V versus RHE, under illumination. (c) Plot of the effect of oxygen isotopic variation on the infrared absorption spectra during PEC water oxidation with hematite electrodes. Reproduced with permission from ref. [91]. Copy right 2016 Springer Nature. (d) FT-IR spectra recorded on the hematite photoanode under AM 1.5 G illumination with applied potential of 1.6 VRHE at different pHs. (e) Relationship of photocurrent densities (μA cm^{-2}) and surface hole densities (number of holes nm^{-2}) at pH

10.0 (black square) and pH 13.6 (red dot). (f) Schematic of the O-O bond formation path way transition with electrolyte pH. Reproduced with permission from ref. [99]. Copy right 2018 American Chemical Society.

$K_4[Fe(CN)_6]$, the reaction order keeps constant as 1 with increasing hole concentration.[102] The third order reaction of PEC water oxidation is explained by the rate-limiting step of forming an intermediate requiring three-hole incorporation.[71] These conclusions are consistent with a recent theoretical calculation work which suggests that the key to enhancing the photocatalytic OER efficiency is to increase the concentration of surface holes.[104] Inspired by the rate law analysis, the water oxidation kinetics on photoanodes was efficiently promoted by increasing the surface hole concentration through strategies such as doping and coating hole-storing overlayers.[105]

Furthermore, the PIA technique was applied to investigate the role of ECs on photoanodes. The hole accumulation in CoPi was quantified for a CoPi/$BiVO_4$ photoanode.[106] When apparent photocurrent is observed on $BiVO_4$/CoPi, the hole concentration in CoPi is too low to contribute noticeable current, indicating that hole transfer from $BiVO_4$ to CoPi is not efficient. Hence, the authors concluded that water oxidation on CoPi/$BiVO_4$ occurs primarily on $BiVO_4$ rather than CoPi.[106] In comparison, CoFe-Prussian blue (PB)/$BiVO_4$ can provide a more favourable interface for efficient hole transfer, which can be inferred from the change of PIA spectrum induced by CoFe-PB modification (Figure 9d).[107]

3.2 Transient absorption spectroscopy (TAS)

TAS is generally used to study the time scale of fundamental processes in solar energy conversion, including formation, trapping, transfer, and recombination of photogenerated charge carriers in semiconductors.[108-110] TAS is based on the pump-probe technique, where the pump initiates the photoexcitation of a sample and the probe measures the optical absorption of the sample at various time following the excitation, thus tracing the time evolution from excited states to ground states.[111]

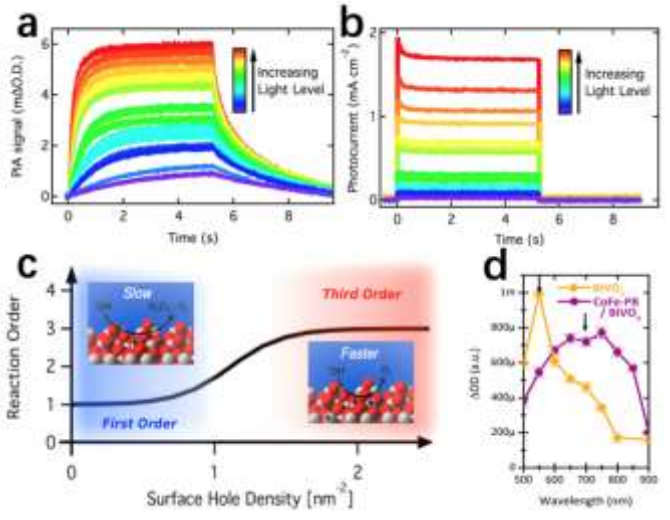

Figure 9. (a) The PIA signals recorded at 650 nm and (b) the photocurrent densities measured simultaneously, with the sample being held at 1.5 V_{RHE} in 1 M NaOH electrolyte. (c) Transition of water oxidation reaction order from 1 to 3 with increasing surface hole density on hematite photoanodes. Reproduced with permission from ref. [71]. Copy right 2015 American Chemical Society. (d) Comparison of PIA spectra of CoFe-PB modified and unmodified $BiVO_4$. Reproduced with permission from ref. [107]. Copy right 2018 American Chemical Society.

In situ TAS measurement under PEC conditions enables the direct observation of the photogenerated carrier kinetics in photoelectrodes, and the spectra should be collected in the time range matching the time scale of the kinetic process of interest. Generally, charge transfer at solid-liquid interfaces exhibits slower kinetics (longer time scales) than that at solid-solid interfaces.

3.2.1 TAS in µs-s. TAS spectra in µs-s timescale are conventionally collected using a laser flash photolysis (LFP) spectrometer, where the pump is provided by a ns-laser and the probe is provided by a flash lamp.[112,113] The time resolution of LFP spectrometers are determined by the sensitivity of detectors. Systematic studies on the photoanode-electrolyte interfacial charge behaviour and the water oxidation kinetics have been carried out by using µs-s TAS.[101,114-116] Taking hematite as the study platform, Durant and coworkers observed a general potential-dependent feature on the TAS spectra of hematite photoanodes regardless of the fabrication methods.[92,101] The positive TAS peak at 580 nm under unbiased condition turns to a bleaching (negative) peak under anodic applied bias (Figure 10a). The 580 nm TAS signal was assigned to an intraband trap states. The peak transition from positive to negative can be ascribed to emptying the initially electron-occupied trap states by anodic applied bias, which is consistent with the growing space charge layer width with positive potentials.[117] It was suggested that the trap states can trap electrons to the photoanode surface and induce back reaction for oxygen reduction or surface charge recombination.[118,119] As indicated by the TAS study from Li and coworkers, an acid treatment on hematite can increase the de-trapping rate of trapped electrons, thus alleviating the losses of photoelectrons at the photoanode-electrolyte interface.[118] Besides, a broad photoinduced absorption peaking at 650 nm (Figure 10a) with a timescale of ms-s is observed when applying positive voltages, while it is absent when the film is near flat-band potential or under unbiased conditions.[101,120] The authors assigned this transient absorption signal to photogenerated holes in hematite and gave interpretation as follows. The increasing band bending of hematite with anodic potentials results in less charge recombination in the space charge region, thus photogenerated holes accumulate near the hematite surface, giving rise to the broad absorption band of photoholes.[101] The dynamics of the transient absorption probed at 650 nm shows a clear biphasic decay (Figure 10b), with a relatively fast decay within 10 ms that can be assigned to electron-hole recombination, and a slower decay that extends to ~1 s which corresponds to long-lived photoholes.[100] The amplitude of TAS signal for the long-lived photoholes increases with applied bias,

exhibiting a similar threshold potential and bias-dependence as compared to the photocurrent-potential curve (Figure 10c).[100] This quantitative correlation indicates that the PEC water oxidation occurs in the timescale of ~1 s, and thus accumulation of long-lived photoholes is a prerequisite to the observation of water oxidation photocurrent. Moreover, it is suggested that the consumption of the long-lived photoholes is a combined process of PEC water oxidation and back electron-hole recombination across the space charge layer.[121] The two processes were distinguished by combining TAS with photocurrent transient and PEIS measurements, and the rate constants were calculated to be 0.5 s^{-1} for water oxidation and 100-1 s^{-1} for back electron-hole recombination, respectively. The results indicate that back electron-hole recombination is strongly competing with water oxidation at the photoanode-electrolyte interface (Figure 10d), causing significant efficiency loss of water splitting photonaodes.[121]

Furthermore, μs-s TAS was also used to interrogate the water oxidation-relevant carrier dynamics influenced by electrocatalysts, passivation overlayers, or heterojunctions. CoPi can form Schottky-type junction with hematite, and GeO_x can passivate the surface states of hematite, both of which increase band bending and electron depletion in hematite, inhibiting back electron-hole recombination.[92,120] Besides, WO_3 can efficiently extract electrons from $BiVO_4$, which benefits the yield and accumulation of long-lived holes on $BiVO_4$ surface.[122,123] In these cases, TAS measurements indicate an elongated lifetime of surface holes in the composite photoanodes as compared to that in the bare ones, thus leading to promoted water oxidation and enhanced photocurrents.

3.2.2 Ultrafast TAS. TAS in ps and fs time domains is a powerful and sensitive tool to investigate the ultrafast photochemical and photophysical dynamics. Temporal evolution of the transient excited states is collected by measuring the absorption at different time delays between pump and probe pulses.[111] Typically, both pump and probe

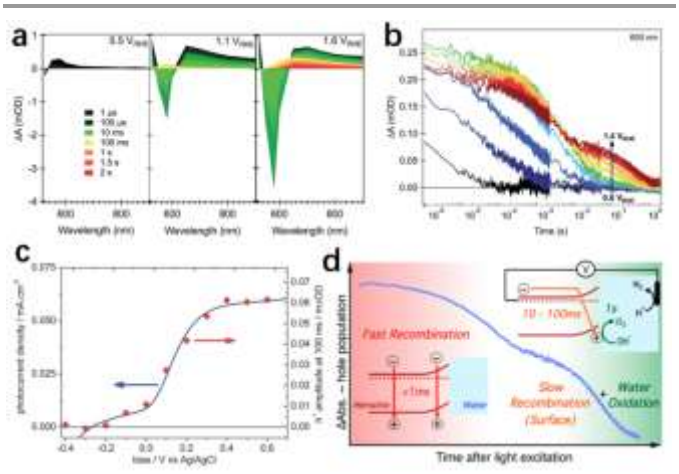

Figure 10. (a) Transient absorption spectra of nanostructured Si-doped CVD hematite photoanodes under different applied electrical bias relative to RHE in 0.1 M NaOH. (b) Effect of applied electrical bias in the transient absorption decay dynamics of nanostructured hematite photoanodes probed at 650 nm after bandgap excitation with 355 nm laser light. Reproduced with permission from ref. [101]. Copyright 2013 The Royal Society of Chemistry. (c) Correlation of the photocurrent density (dark blue line) with the long-lived photohole signal amplitude at 100 ms (red diamonds) as a function of applied electrical bias. Reproduced with permission from ref. [100]. Copyright 2012 The Royal Society of Chemistry. (d) Illustration of the charge recombination and surface water oxidation time scales inferred from TAS decay. Reproduced with permission from ref. [121]. Copyright 2014 American Chemical Society.

pulses are generated by fs-lasers, and the time delay between the two pulses can be continuously varied by using an optical delay line.[111,124] The maximum measured time scale is several nanoseconds due to the space limitation of the optical delay line.

Constructing SC-SC heterojunctions has been a widely utilized strategy towards more efficient photoelectrodes.[16,125] The improved PEC activity of the heterojunctions as compared to their monocomponent counterparts can be ascribed to the internal electric field which benefits charge separation, or the combination of advantages from different semiconductors.[16,126] However, understanding the detailed carrier dynamics at a heterojunction is difficult, since techniques with sufficiently high time resolution is required to monitor the ultrafast process occurs at solid-solid interfaces.[127] Thanks to the development of ultrafast TAS, researchers recently are getting deeper understanding on the interfacial charge behaviour at the heterojunctions between semiconductors.

$BiVO_4/WO_3$ is one of the most studied platforms of SC-SC heterojunction photoanodes with type-II band alignment, which can simultaneously utilize the good visible light response of $BiVO_4$ and the excellent electronic conductivity of WO_3, thus leading to the significantly enhanced PEC activity.[125,128] Systematic studies by using ultrafast TAS have been carried out to elucidate the interfacial charge behaviour in $BiVO_4/WO_3$ heterojunction.

Initially, the ultrafast TAS measurement were performed under non-operando conditions. UV-visible pulses were suggested to be valid probe for photoexcited holes in $BiVO_4$, and thus the electron injection from $BiVO_4$ to WO_3 was inferred by detecting the $BiVO_4$ hole dynamics by using ultrafast TAS in UV-visible region.[129-131] Furthermore, Selli's group demonstrated that photoexcited electrons can be directly monitored by midinfrared (IR) probes.[127] The time-resolved IR TAS traces recorded for monocomponent semiconductors are displayed in Figure 11a, demonstrating that photogenerated electrons live much longer in WO_3 (red circle) than in $BiVO_4$ (blue square). When the $BiVO_4/WO_3$ heterojunction is excited upon 500 nm pump, photocarriers generate only in $BiVO_4$ but not in WO_3 since the excitation energy is higher than the band gap of $BiVO_4$ but lower than that of WO_3. The IR TAS signal of photoelectrons in $BiVO_4/WO_3$ heterojunction upon the exclusive excitation of $BiVO_4$ exhibits very a similar decay trace (Figure 11a, green triangle) with the that in the single WO_3 (Figure 11a, red circle). The decay traces were further analysed by fitting with exponential equations for time constant calculation, suggesting that the electron transfer from $BiVO_4$ to WO_3 is ultrafast (Figure 11b) and even faster than the function response of the experimental setup (~200 fs). Consistently, Durrant *et al* also manifested the faster electron injection from $BiVO_4$ into WO_3 than that into FTO substrate. When the $BiVO_4/WO_3$ heterojunction is excited by 410 nm pump, photocarriers simultaneously generate in both semiconductors, activating the

pathway of recombination between holes in $BiVO_4$ and electrons in WO_3 (Figure 11b), thus shortening the lifetime of photogenerated carriers (Figure 11a, orange star). This work provides direct evidence for the fast electron transfer at the $BiVO_4/WO_3$ interface. It is also suggested that future efforts

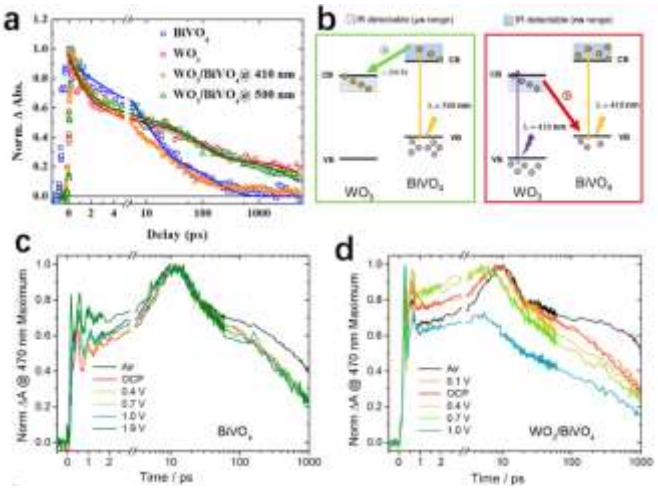

Figure 11. (a) IR-fs TA traces recorded at 2050 cm^{-1} with the WO_3 (red circles), $BiVO_4$ (blue squares), and $WO_3/BiVO_4$ (orange stars) electrodes upon 410 nm excitation (270 nJ/pulse) and with $WO_3/BiVO_4$ upon 500 nm excitation (300 nJ/pulse; green triangles). (b) Excitation wavelength dependent electronic interactions in $WO_3/BiVO_4$ under selective excitation of $BiVO_4$ (500 nm pump) and simultaneous excitation of both oxides (410 nm pump). Reproduced with permission from ref. [127]. Copyright 2018 American Chemical Society. Ultrafast TAS dynamics of (c) $BiVO_4$ and (d) $WO_3/BiVO_4$ monitored at 470 nm. Reproduced with permission from ref. [132] Copyright 2019 American Chemical Society.

should be paid on minimizing the parasitic interfacial charge recombination upon simultaneous excitation, thus to further improve the performance of the heterojunction photoanode.[127]

Furthermore, Selli's group conducted operando UV-visible fs-TAS of $BiVO_4/WO_3$ photoanode under PEC conditions, finding that the TAS trace of $BiVO_4/WO_3$ shows a more pronounced bias-dependence compared with that of bare $BiVO_4$ (Figure 11c and 11d), which can be ascribed to the built-in electric field at the heterojunction.[132] Combining electronic measurements, they concluded that the bias-altered intraband gaps states in $BiVO_4$ play a critical role in determining the carrier dynamics of $BiVO_4/WO_3$ heterojunction.[132]

Optical techniques are used not as widely as electrochemical techniques in PEC studies, which is mainly due to the difficulty of performing in situ optical spectroscopic measurements under operative PEC conditions.[133] It is also challenging to collect accurate information from the complex reaction environment that combines illumination, applied bias, and solution. Besides, the complicated setup of optical paths and the high expense of lasers in TAS also hinders the wide application. However, optical techniques are indispensable for deep understanding of the PEC mechanisms since they can provide important information which is not accessible by electrochemical techniques. The functions and weaknesses of the introduced optical techniques are briefly listed in Table 3.

4. Summary and perspectives

Techniques applied for the interface study in PEC systems are overviewed herein. In the electrochemical technique section, we introduced PEIS and IMPS for interrogation of interfacial charge transfer and recombination, OCP for photovoltage measurement, CV and chopped-light CA for observation of interfacial charge accumulation, as well as the DWE technique for SC/EC interface investigation. In the optical spectroscopic technique section, steady sate optical spectroscopy is first introduced, including spectroelectrochemistry and ATR-IR spectroscopy which are mainly used for reaction intermediate detection, as well as PIA technique which aims at hole quantification at operative PEC conditions. Besides, transient absorption spectroscopy that traces the time evolution of photocarriers is also introduced, including μs-s TAS for solid-solution interfaces and fs-ps TAS for solid-solid interfaces. Insightful understandings have been gleaned on the SC-electrolyte, SC-EC, and SC-SC interfaces during PEC process, including interfacial thermodynamics, carrier dynamics, as well as the water oxidation kinetics and pathways. However, challenges still remain, and much efforts should be paid on the

Table 3. A summary and comparison of optical spectroscopic techniques for interface study in PEC systems.

Technique	Outputs	Weaknesses	Ref.
Spectroelect-rochemistry	Reaction intermediate detection	Cannot provide the accurate chemical identity of the intermediate species.	91,95
ATR-IR	Reaction intermediate identification and reaction pathway study	IR absorption of electrolyte can disturb the analysis. Ultrathin layer of electrolyte within a micrometre is required.	91,99
PIA	Quantification of charge accumulation at operative PEC conditions Rate law measurement	Holes in EC and SC may not be accurately distinguished in a composite photoanode.	71
TAS	μs-s TAS for solid-solution interfacial carrier dynamics Ultrafast TAS for solid-solid interfacial carrier dynamics	Intense excitation pulse is required to generate detectable signals, which deviates from continuous solar irradiation.	100

future development of techniques for in-depth PEC interface study.

First, the data reliability should be cautiously evaluated and validated. Some methods relying on too much prior assumptions and models have limited application only for certain conditions. Specifically, for PEIS and IMPS, the characteristic frequency assignment, the equivalent circuit establishment, and the rate constant calculation require sufficient prior knowledge on the studying systems, and thus should be conducted carefully. Such analysis may heedlessly spread to inappropriate situations and cause misleading conclusions. Hence, development of techniques with direct observation and straightforward data interpretation is encouraged, since they give more reliable evidences and have more potential to be widely applicable.

Second, employing different techniques on one experimental system is good way to address the validity issue, as well as to gain deeper mechanistic understanding. For instance, both electrochemical and optical spectroscopic techniques can be simultaneously utilized to confirm the time scale of interfacial charge behaviour, or the energetics of some interface defects and trap states.[93,121] Besides, by analysing the electronic response of photoelectrodes accompanied by the chemical identity determination of intermediate species, the detailed interfacial charge transfer steps might be inferred.[99] Hence, combining the complementary information obtained from different techniques allows more comprehensive knowledge of the underlying mechanisms.

Third, new in situ techniques should be explored for PEC studies towards characterization in nanoscale and even atomic scale. Nanostructured photoelectrodes are always favoured due to the higher PEC activity. However, the heterogeneity of physicochemical property at nanoscale adds to the difficulty of interface study. Conventional electrochemical responses are collected for the photoelectrode as a whole, where the interfaces in the multilayer photoanode cannot be directly distinguished. In contrast, the newly-developed DWE technique provides direct and independent observation of the potential and current on the SC and the EC in an SC/EC composite photoanode, and thus junction photovoltages and charge accumulation in the EC can be directly detected at operative PEC conditions. More excitingly, the spatial resolution in PEC study is improved to nanoscale by using the AFM tip-based DEW technique. However, this single powerful DWE technique is not enough, more various techniques with high spatial resolution is demanded. For instance, space-resolved surface photovoltage (SPV) has been implemented in photocatalysis field to map the separation of photogenerated carriers dominated by the facet exposure and defect distribution at nanoscale in a photocatalyst.[134,135] This SPV technique is also expected to be applied in PEC field to deliver useful information. Furthermore, in situ transmission electron spectroscopy, which have been implemented in electrocatalysis and photocatalysis field, is also suggested to be utilized in PEC study.[136-138] It would enable researchers to directly observe the structure evolution of materials at atomic scale under operative conditions, thus helping to construct the structure-performance relationship and guide the design of highly efficient photoelectrodes.

Fourth, theoretical simulation/modelling should be combined with experimental techniques to obtain insightful

understanding on PEC systems. By conducting the optical modelling in company with photocurrent action spectra measurements on planar photoelectrodes, Sharp *et al.* extracted the spatial collection efficiency (SCE) during PEC process. The modeling should be carried out carefully especially for transition metal oxide semiconductors, where the generation of photocarriers can be affected by the electronic transition type in addition to light absorption. The SCE profiles enabled the researchers to quantify the efficiency losses coming from bulk and surface of a photoelectrode. It also helped to differentiate the performance bottlenecks, which is meaningful for photoelectrode modification.[139,140] Beside the simulation of optical and electronic properties within the semiconductors as introduced above, simulation of the electrode-electrolyte interface, as well as the mass transport in the electrolyte, are also important and should be considered in the future study.

In summary, the in-depth understanding of PEC interfaces is essentially dependent on the advances of study techniques. Although the existing techniques have guided great progress, challenges regarding the data reliability, spatial and time resolution, and the difficulty of in situ characterization, still remains to be overcome. Exploiting new techniques, cooperation between different techniques, and the addition of theoretical simulations, may hold the opportunity for new breakthrough of mechanistic study, thus allowing further efficiency improvement of PEC cells.

Conflicts of interest

There are no conflicts to declare.

Acknowledgements

P. Tan thanks the funding support from CAS Pioneer Hundred Talents Program (KJ2090130001), USTC Research Funds of the Double First-Class Initiative (YD2090002006), Joint Laboratory for USTC and Yanchang Petroleum (ES2090130110), and USTC Tang Scholar. Y. DAI thanks the PhD Fellowship from the Research Grant Council, University Grants Committee, Hong Kong SAR.

References

1. P. Zhang, T. Wang, X. Chang and J. Gong, *Acc. Chem. Res.*, 2016, **49**, 911-921.
2. I. Roger, M. A. Shipman and M. D. Symes, *Nat. Rev. Chem.*, 2017, **1**, 0003.
3. T. Hisatomi, J. Kubota and K. Domen, *Chem. Soc. Rev.*, 2014, **43**, 7520-7535.
4. X. Chen, S. Shen, L. Guo and S. S. Mao, *Chem. Rev.*, 2010, **110**, 6503-6570.
5. J. H. Kim, D. Hansora, P. Sharma, J.-W. Jang and J. S. Lee, *Chem. Soc. Rev.*, 2019, **48**, 1908-1971.
6. K. Zhang, M. Ma, P. Li, D. H. Wang and J. H. Park, *Adv. Energy Mater.*, 2016, **6**, 1600602.
7. H. Kobayashi, N. Sato, M. Orita, Y. Kuang, H. Kaneko, T. Minegishi, T. Yamada and K. Domen, *Energy Environ. Sci.*, 2018, **11**, 3003-3009.
8. C. Li, Z. Luo, T. Wang and J. Gong, *Adv. Mater.*, 2018, **30**, 1707502.
9. F. Lin and S. W. Boettcher, *Nat. Mater.*, 2014, **13**, 81.
10. D. Bae, B. Seger, P. C. Vesborg, O. Hansen and I. Chorkendorff, *Chem. Soc. Rev.*, 2017, **46**, 1933-1954.
11. M. G. Ahmed, I. E. Kretschmer, T. A. Kandiel, A. Y. Ahmed, F. A. Rashwan and D. W. Bahnemann, *ACS Appl. Mater. Interfaces*, 2015, **7**, 24053-24062.
12. I. A. Digdaya, G. W. Adhyaksa, B. J. Trześniewski, E. C. Garnett and W. A. Smith, *Nat. Commun.*, 2017, **8**, 15968.
13. K. Sivula, *J. Phys. Chem. Lett.*, 2013, **4**, 1624-1633.
14. O. Zandi and T. W. Hamann, *J. Phys. Chem. Lett.*, 2014, **5**, 1522-1526.
15. K. Zhang, Y. Dai, Z. Zhou, S. U. Jan, L. Guo and J. R. Gong, *Nano Energy*, 2017, **41**, 101-108.
16. S. Shen, S. A. Lindley, X. Chen and J. Z. Zhang, *Energy Environ. Sci.*, 2016, **9**, 2744-2775.
17. C. Ding, J. Shi, Z. Wang and C. Li, *ACS Catal.*, 2016, **7**, 675-688.
18. Y. Dai, P. Cheng, G. Xie, C. Li, M. Z. Akram, B. Guo, R. Boddula, X. Shi, J. Gong and J. R. Gong, *J. Phys. Chem. C*, 2019, **123**, 28753-28762.
19. Y. Kuang, T. Yamada and K. Domen, *Joule*, 2017, **1**, 290-305.
20. P. Zhang, T. Wang and J. Gong, *Chem*, 2018, **4**, 223-245.
21. M. R. Nellist, F. A. Laskowski, F. Lin, T. J. Mills and S. W. Boettcher, *Acc. Chem. Res.*, 2016, **49**, 733-740.
22. K. M. Young, B. M. Klahr, O. Zandi and T. W. Hamann, *Catal. Sci. Technol.*, 2013, **3**, 1660-1671.
23. A. J. Bard, L. R. Faulkner, J. Leddy and C. G. Zoski, *Electrochemical methods: fundamentals and applications*, Wiley, New York, 1980.
24. B. Klahr, S. Gimenez, F. Fabregat-Santiago, J. Bisquert and T. W. Hamann, *Energy Environ. Sci.*, 2012, **5**, 7626-7636.
25. D. Klotz, D. S. Ellis, H. Dotan and A. Rothschild, *Phys. Chem. Chem. Phys.*, 2016, **18**, 23438-23457.
26. F. Malara, A. Minguzzi, M. Marelli, S. Morandi, R. Psaro, V. Dal Santo and A. Naldoni, *ACS Catal.*, 2015, **5**, 5292-5300.
27. Y. Zhang, H. Zhang, H. Ji, W. Ma, C. Chen and J. Zhao, *J. Am. Chem. Soc.*, 2016, **138**, 2705-2711.
28. G. Xie, S. U. Jan, Z. Dong, Y. Dai, R. Boddula, Y. Wei, C. Zhao, Q. Xin, J.-N. Wang and Y. Du, *Chin. J. Catal.*, 2020, **41**, 2-8.
29. L. Wang, N. T. Nguyen, Z. Shen, P. Schmuki and Y. Bi, *Nano Energy*, 2018, **50**, 331-338.
30. F. Malara, F. Fabbri, M. Marelli and A. Naldoni, *ACS Catal.*, 2016, **6**, 3619-3628.
31. K. Zhang, T. Dong, G. Xie, L. Guan, B. Guo, Q. Xiang, Y. Dai, L. Tian, A. Batool and S. U. Jan, *ACS Appl. Mater. Interfaces*, 2017, **9**, 42723-42733.
32. F. Li, J. Li, L. Gao, Y. Hu, X. Long, S. Wei, C. Wang, J. Jin and J. Ma, *J. Mater. Chem. A*, 2018, **6**, 23478-23485.
33. L. Bertoluzzi and J. Bisquert, *J. Phys. Chem. Lett.*, 2012, **3**, 2517-2522.
34. B. Klahr, S. Gimenez, F. Fabregat-Santiago, T. Hamann and J. Bisquert, *J. Am. Chem. Soc.*, 2012, **134**, 4294-4302.
35. D. Monllor-Satoca, M. Bärtsch, C. Fabrega, A. Genç, S. Reinhard, T. Andreu, J. Arbiol, M. Niederberger and J. R. Morante, *Energy Environ. Sci.*, 2015, **8**, 3242-3254.

36. B. Klahr, S. Gimenez, F. Fabregat-Santiago, J. Bisquert and T. W. Hamann, *J. Am. Chem. Soc.*, 2012, **134**, 16693-16700.
37. H. Hajibabaei, A. R. Schon and T. W. Hamann, *Chem. Mater.*, 2017, **29**, 6674-6683.
38. H.-J. Lewerenz and L. Peter, *Photoelectrochemical water splitting: materials, processes and architectures*, Royal Society of Chemistry, Cambridge, 2013.
39. J. Zhang, R. García-Rodríguez, P. Cameron and S. Eslava, *Energy Environ. Sci.*, 2018, **11**, 2972-2984.
40. K. U. Wijayantha, S. Saremi-Yarahmadi and L. M. Peter, *Phys. Chem. Chem. Phys.*, 2011, **13**, 5264-5270.
41. G. M. Carroll and D. R. Gamelin, *J. Mater. Chem. A*, 2016, **4**, 2986-2994.
42. L. Peter and D. Vanmaekelbergh, *Adv. Electrochem. Sci. Eng.*, 1999, **6**, 77-164.
43. J. Krüger, R. Plass, M. Grätzel, P. J. Cameron and L. M. Peter, *J. Phys. Chem. B*, 2003, **107**, 7536-7539.
44. G. Canning, A. K. Thomas, D. H. Dunlap and J. K. Grey, *ACS Appl. Mater. Interfaces*, 2018, **10**, 19853-19862.
45. J. H. Heo, D. H. Shin, D. H. Song, D. H. Kim, S. J. Lee and S. H. Im, *J. Mater. Chem. A*, 2018, **6**, 8251-8258.
46. Y. Liu, F. Le Formal, F. Boudoire, L. Yao, K. Sivula and N. Guijarro, *J. Mater. Chem. A*, 2019, **7**, 1669-1677.
47. J. E. Thorne, J.-W. Jang, E. Y. Liu and D. Wang, *Chem. Sci.*, 2016, **7**, 3347-3354.
48. C. Zachäus, F. F. Abdi, L. M. Peter and R. Van De Krol, *Chem. Sci.*, 2017, **8**, 3712-3719.
49. L. M. Peter, *Chem. Rev.*, 1990, **90**, 753-769.
50. L. M. Peter, *J. Solid State Electrochem.*, 2013, **17**, 315-326.
51. L. M. Peter, K. U. Wijayantha and A. A. Tahir, *Faraday Discuss.*, 2012, **155**, 309-322.
52. D. Klotz, D. A. Grave and A. Rothschild, *Phys. Chem. Chem. Phys.*, 2017, **19**, 20383-20392.
53. W. W. Gärtner, *Phys. Rev.*, 1959, **116**, 84.
54. J. B. Sambur, T.-Y. Chen, E. Choudhary, G. Chen, E. J. Nissen, E. M. Thomas, N. Zou and P. Chen, *Nature*, 2016, **530**, 77-80.
55. W. Li, D. He, S. W. Sheehan, Y. He, J. E. Thorne, X. Yao, G. W. Brudvig and D. Wang, *Energy Environ. Sci.*, 2016, **9**, 1794-1802.
56. F. A. Laskowski, M. R. Nellist, J. Qiu and S. W. Boettcher, *J. Am. Chem. Soc.*, 2018, **141**, 1394-1405.
57. A. Tsyganok, D. Klotz, K. D. Malviya, A. Rothschild and D. A. Grave, *ACS Catal.*, 2018, **8**, 2754-2759.
58. Z. Chen, H. N. Dinh and E. Miller, *Photoelectrochemical water splitting*, Springer, New York, 2013.
59. Z. Xu, H. Wang, Y. Wen, W. Li, C. Sun, Y. He, Z. Shi, L. Pei, Y. Chen and S. Yan, *ACS Appl. Mater. Interfaces*, 2018, **10**, 3624-3633.
60. M. T. Mayer, *Curr. Opin. Electrochem.*, 2017, **2**, 104-110.
61. J. E. Thorne, S. Li, C. Du, G. Qin and D. Wang, *J. Phys. Chem. Lett.*, 2015, **6**, 4083-4088.
62. X. Yang, C. Du, R. Liu, J. Xie and D. Wang, *J. Catal.*, 2013, **304**, 86-91.
63. Y. Lin, Y. Xu, M. T. Mayer, Z. I. Simpson, G. McMahon, S. Zhou and D. Wang, *J. Am. Chem. Soc.*, 2012, **134**, 5508-5511.
64. C. Du, X. Yang, M. T. Mayer, H. Hoyt, J. Xie, G. McMahon, G. Bischoping and D. Wang, *Angew. Chem. Int. Ed.*, 2013, **52**, 12692-12695.
65. X. Yang, R. Liu, C. Du, P. Dai, Z. Zheng and D. Wang, *ACS Appl. Mater. Interfaces*, 2014, **6**, 12005-12011.
66. M. Forster, R. J. Potter, Y. Yang, Y. Li and A. J. Cowan, *ChemPhotoChem*, 2018, **2**, 183-189.
67. T. Li, J. He, B. Peña and C. P. Berlinguette, *Angew. Chem. Int. Ed.*, 2016, **55**, 1769-1772.
68. J.-W. Jang, C. Du, Y. Ye, Y. Lin, X. Yao, J. Thorne, E. Liu, G. McMahon, J. Zhu and A. Javey, *Nat. Commun.*, 2015, **6**, 7447.
69. H. Dotan, K. Sivula, M. Grätzel, A. Rothschild and S. C. Warren, *Energy Environ. Sci.*, 2011, **4**, 958-964.
70. G. Liu, J. Shi, F. Zhang, Z. Chen, J. Han, C. Ding, S. Chen, Z. Wang, H. Han and C. Li, *Angew. Chem. Int. Ed.*, 2014, **53**, 7295-7299.
71. F. Le Formal, E. Pastor, S. D. Tilley, C. A. Mesa, S. R. Pendlebury, M. Grätzel and J. R. Durrant, *J. Am. Chem. Soc.*, 2015, **137**, 6629-6637.
72. Y. Gao and T. W. Hamann, *J. Phys. Chem. Lett.*, 2017, **8**, 2700-2704.
73. G. Liu, S. Ye, P. Yan, F. Xiong, P. Fu, Z. Wang, Z. Chen, J. Shi and C. Li, *Energy Environ. Sci.*, 2016, **9**, 1327-1334.
74. S. Ye, C. Ding, R. Chen, F. Fan, P. Fu, H. Yin, X. Wang, Z. Wang, P. Du and C. Li, *J. Am. Chem. Soc.*, 2018, **140**, 3250-3256.
75. C. Cui, M. Heggen, W.-D. Zabka, W. Cui, J. Osterwalder, B. Probst and R. Alberto, *Nat. Commun.*, 2017, **8**, 1341.
76. Z. Wang, G. Liu, C. Ding, Z. Chen, F. Zhang, J. Shi and C. Li, *J. Phys. Chem. C*, 2015, **119**, 19607-19612.
77. J. Qiu, H. Hajibabaei, M. R. Nellist, F. A. Laskowski, T. W. Hamann and S. W. Boettcher, *ACS Cent. Sci.*, 2017, **3**, 1015-1025.
78. F. A. Laskowski, M. R. Nellist, R. Venkatkarthick and S. W. Boettcher, *Energy Environ. Sci.*, 2017, **10**, 570-579.
79. F. A. Laskowski, J. Qiu, M. R. Nellist, S. Z. Oener, A. M. Gordon and S. W. Boettcher, *Sustain. Energy Fuels*, 2018, **2**, 1995-2005.
80. R. C. Rossi, M. X. Tan and N. S. Lewis, *Appl. Phys. Lett.*, 2000, **77**, 2698-2700.
81. J. Qiu, H. Hajibabaei, M. R. Nellist, F. A. Laskowski, S. Z. Oener, T. W. Hamann and S. W. Boettcher, *ACS Energy Lett.*, 2018, **3**, 961-969.
82. J. Deng, M. R. Nellist, M. B. Stevens, C. Dette, Y. Wang and S. W. Boettcher, *Nano Lett.*, 2017, **17**, 6922-6926.
83. M. R. Nellist, F. A. Laskowski, J. Qiu, H. Hajibabaei, K. Sivula, T. W. Hamann and S. W. Boettcher, *Nat. Energy*, 2018, **3**, 46.
84. M. R. Nellist, J. Qiu, F. A. Laskowski, F. M. Toma and S. W. Boettcher, *ACS Energy Lett.*, 2018, **3**, 2286-2291.
85. F. A. Laskowski, S. Z. Oener, M. R. Nellist, A. M. Gordon, D. C. Bain, J. L. Fehrs and S. W. Boettcher, *Nat. Mater.*, 2019, 1-8.
86. J. Eichhorn, C. Kastl, J. K. Cooper, D. Ziegler, A. M. Schwartzberg, I. D. Sharp and F. M. Toma, *Nat. Commun.*, 2018, **9**, 1-8.
87. G. Liu, J. Eichhorn, C.-M. Jiang, M. C. Scott, L. H. Hess, J. M. Gregoire, J. A. Haber, I. D. Sharp and F. M. Toma, *Sustain. Energy Fuels*, 2019, **3**, 127-135.
88. C. Y. Cummings, F. Marken, L. M. Peter, A. A. Tahir and K. U. Wijayantha, *Chem. Commun.*, 2012, **48**, 2027-2029.
89. C. Y. Cummings, F. Marken, L. M. Peter, K. Upul Wijayantha and A. A. Tahir, *J. Am. Chem. Soc.*, 2011, **134**, 1228-1234.
90. B. Klahr and T. Hamann, *J. Phys. Chem. C*, 2014, **118**, 10393-10399.
91. O. Zandi and T. W. Hamann, *Nat. Chem.*, 2016, **8**, 778.
92. M. Barroso, C. A. Mesa, S. R. Pendlebury, A. J. Cowan, T. Hisatomi, K. Sivula, M. Grätzel, D. R. Klug and J. R. Durrant, *Proc. Natl. Acad. Sci.*, 2012, **109**, 15640-15645.
93. S. Selim, E. Pastor, M. García-Tecedor, M. R. Morris, L. Francas, M. Sachs, B. Moss, S. Corby, C. A. Mesa and S. Gimenez, *J. Am. Chem. Soc.*, 2019.
94. F. T. De Oliveira, A. Chanda, D. Banerjee, X. Shan, S. Mondal, L. Que, E. L. Bominaar, E. Münck and T. J. Collins, *Science*, 2007, **315**, 835-838.

95. T. Takashima, K. Ishikawa and H. Irie, *J. Phys. Chem. C*, 2016, **120**, 24827-24834.
96. B. Iandolo and A. Hellman, *Angew. Chem. Int. Ed.*, 2014, **53**, 13404-13408.
97. P. Elmer, *Technical note*, 2005, **27**.
98. F. M. Mirabella, *Internal reflection spectroscopy: Theory and applications*, CRC Press, New York, 1992.
99. Y. Zhang, H. Zhang, A. Liu, C. Chen, W. Song and J. Zhao, *J. Am. Chem. Soc.*, 2018, **140**, 3264-3269.
100. S. R. Pendlebury, A. J. Cowan, M. Barroso, K. Sivula, J. Ye, M. Grätzel, D. R. Klug, J. Tang and J. R. Durrant, *Energy Environ. Sci.*, 2012, **5**, 6304-6312.
101. M. Barroso, S. R. Pendlebury, A. J. Cowan and J. R. Durrant, *Chem. Sci.*, 2013, **4**, 2724-2734.
102. Y. Ma, C. A. Mesa, E. Pastor, A. Kafizas, L. Francàs, F. Le Formal, S. R. Pendlebury and J. R. Durrant, *ACS Energy Lett.*, 2016, **1**, 618-623.
103. A. Kafizas, Y. Ma, E. Pastor, S. R. Pendlebury, C. Mesa, L. Francàs, F. Le Formal, N. Noor, M. Ling and C. Sotelo-Vazquez, *ACS Catal.*, 2017, **7**, 4896-4903.
104. D. Wang, T. Sheng, J. Chen, H.-F. Wang and P. Hu, *Nat. Catal.*, 2018, **1**, 291-299.
105. A. J. Abel, A. M. Patel, S. Y. Smolin, B. Opasanont and J. B. Baxter, *J. Mater. Chem. A*, 2016, **4**, 6495-6504.
106. Y. Ma, A. Kafizas, S. R. Pendlebury, F. Le Formal and J. R. Durrant, *Adv. Funct. Mater.*, 2016, **26**, 4951-4960.
107. B. Moss, F. S. Hegner, S. Corby, S. Selim, L. Francàs, N. r. López, S. Giménez, J.-R. n. Galán-Mascarós and J. R. Durrant, *ACS Energy Lett.*, 2018, **4**, 337-342.
108. J. Schneider and D. Bahnemann, *J. Phys. Chem. C*, 2018, **122**, 13979-13985.
109. C. S. Ponseca Jr, P. Chabera, J. Uhlig, P. Persson and V. Sundstrom, *Chem. Rev.*, 2017, **117**, 10940-11024.
110. R. Qian, H. Zong, J. Schneider, G. Zhou, T. Zhao, Y. Li, J. Yang, D. W. Bahnemann and J. H. Pan, *Catal. Today*, 2019, **335**, 78-90.
111. M. Lorenc, M. Ziolek, R. Naskrecki, J. Karolczak, J. Kubicki and A. Maciejewski, *Appl. Phys. B*, 2002, **74**, 19-27.
112. J. Schneider, K. Nikitin, M. Wark, D. W. Bahnemann and R. Marschall, *Phys. Chem. Chem. Phys.*, 2016, **18**, 10719-10726.
113. M. Usman, S. Mendiratta and K. L. Lu, *Adv. Mater.*, 2017, **29**, 1605071.
114. A. J. Cowan, J. Tang, W. Leng, J. R. Durrant and D. R. Klug, *J. Phys. Chem. C*, 2010, **114**, 4208-4214.
115. S. R. Pendlebury, M. Barroso, A. J. Cowan, K. Sivula, J. Tang, M. Grätzel, D. Klug and J. R. Durrant, *Chem. Commun.*, 2011, **47**, 716-718.
116. J. Tang, J. R. Durrant and D. R. Klug, *J. Am. Chem. Soc.*, 2008, **130**, 13885-13891.
117. S. R. Pendlebury, X. Wang, F. Le Formal, M. Cornuz, A. Kafizas, S. D. Tilley, M. Grätzel and J. R. Durrant, *J. Am. Chem. Soc.*, 2014, **136**, 9854-9857.
118. Y. Yang, M. Forster, Y. Ling, G. Wang, T. Zhai, Y. Tong, A. J. Cowan and Y. Li, *Angew. Chem. Int. Ed.*, 2016, **55**, 3403-3407.
119. D. Cao, W. Luo, J. Feng, X. Zhao, Z. Li and Z. Zou, *Energy Environ. Sci.*, 2014, **7**, 752-759.
120. M. Barroso, A. J. Cowan, S. R. Pendlebury, M. Grätzel, D. R. Klug and J. R. Durrant, *J. Am. Chem. Soc.*, 2011, **133**, 14868-14871.
121. F. Le Formal, S. R. Pendlebury, M. Cornuz, S. D. Tilley, M. Grätzel and J. R. Durrant, *J. Am. Chem. Soc.*, 2014, **136**, 2564-2574.
122. Y. Ma, S. R. Pendlebury, A. Reynal, F. Le Formal and J. R. Durrant, *Chem. Sci.*, 2014, **5**, 2964-2973.
123. S. Selim, L. Francàs, M. García-Tecedor, S. Corby, C. Blackman, S. Gimenez, J. R. Durrant and A. Kafizas, *Chem. Sci.*, 2019, **10**, 2643-2652.
124. A. Maciejewski, R. Naskrecki, M. Lorenc, M. Ziolek, J. Karolczak, J. Kubicki, M. Matysiak and M. Szymanski, *J. Mol. Struct.*, 2000, **555**, 1-13.
125. S. J. Hong, S. Lee, J. S. Jang and J. S. Lee, *Energy Environ. Sci.*, 2011, **4**, 1781-1787.
126. M. T. Mayer, Y. Lin, G. Yuan and D. Wang, *Acc. Chem. Res.*, 2013, **46**, 1558-1566.
127. I. Grigioni, M. Abdellah, A. Corti, M. V. Dozzi, L. Hammarström and E. Selli, *J. Am. Chem. Soc.*, 2018, **140**, 14042-14045.
128. S. Y. Chae, C. S. Lee, H. Jung, O.-S. Joo, B. K. Min, J. H. Kim and Y. J. Hwang, *ACS Appl. Mater. Interfaces*, 2017, **9**, 19780-19790.
129. I. Grigioni, K. G. Stamplecoskie, D. H. Jara, M. V. Dozzi, A. Oriana, G. Cerullo, P. V. Kamat and E. Selli, *ACS Energy Lett.*, 2017, **2**, 1362-1367.
130. I. Grigioni, K. G. Stamplecoskie, E. Selli and P. V. Kamat, *J. Phys. Chem. C*, 2015, **119**, 20792-20800.
131. A. Loiudice, J. K. Cooper, L. H. Hess, T. M. Mattox, I. D. Sharp and R. Buonsanti, *Nano Lett.*, 2015, **15**, 7347-7354.
132. I. Grigioni, L. Ganzer, F. VA Camargo, B. Bozzini, G. Cerullo and E. Selli, *ACS Energy Lett.*, 2019, **4**, 2213-2219.
133. J. Cen, Q. Wu, M. Liu and A. Orlov, *Green Energy Environ.*, 2017, **2**, 100-111.
134. R. Chen, S. Pang, H. An, T. Dittrich, F. Fan and C. Li, *Nano Lett.*, 2018, **19**, 426-432.
135. J. Zhu, S. Pang, T. Dittrich, Y. Gao, W. Nie, J. Cui, R. Chen, H. An, F. Fan and C. Li, *Nano Lett.*, 2017, **17**, 6735-6741.
136. N. Ortiz Peña, D. Ihiawakrim, M. Han, B. Lassalle-Kaiser, S. Carenco, C. Sanchez, C. Laberty-Robert, D. Portehault and O. Ersen, *ACS Nano*, 2019, **13**, 11372-11381.
137. X. Li, H. Y. Wang, H. Yang, W. Cai, S. Liu and B. Liu, *Small Methods*, 2018, **2**, 1700395.
138. Z.-W. Yin, S. B. Betzler, T. Sheng, Q. Zhang, X. Peng, J. Shangguan, K. C. Bustillo, J.-T. Li, S.-G. Sun and H. Zheng, *Nano Energy*, 2019, **62**, 507-512.
139. G. Segev, H. Dotan, D. S. Ellis, Y. Piekner, D. Klotz, J. W. Beeman, J. K. Cooper, D. A. Grave, I. D. Sharp and A. Rothschild, *Joule*, 2018, **2**, 210-224.
140. G. Segev, C.-M. Jiang, J. K. Cooper, J. Eichhorn, F. M. Toma and I. D. Sharp, *Energy Environ. Sci.*, 2018, **11**, 904-913.

